POLITECNICO DI TORINO

Master Degree in Energetic and Nuclear Engineering

Master Degree Thesis

Solid-state glass-ceramic electrolytes for next-generation rechargeable batteries

Supervisors

Prof. Claudio GERBALDI

Prof. Federico SMEACETTO

Candidate

Francesco LA SPINA

OCTOBER 2021

Abstract

Renewable energy sources (RESs) represent a striking energy supply that can help reducing the environmental impact of electricity production. However, some of them (e.g. solar or wind) are intermittent by nature. To overcome this relevant issue, energy storage is an efficient way to maintain a constant electric supply. Batteries used as electrochemical storage represent one of the best solutions.

Solid-state-batteries (SSBs) are devices relying on solid electrolytes to store energy. Their integration to systems based on RESs represent an effective way to overcome their intermittence. This solution is progressively replacing the commonly used liquid electrolytes since they suffer from low thermal stability being volatile and may cause serious safety issues. Furthermore, SSBs offer better cycling stability at lower processing costs. However, SSBs have some intrinsic drawbacks, which include low ionic conductivity and instability at the interface with the electrode materials. Recently, solid electrolytes with a NASICON) structure have been widely investigated by the scientific community, due to their electrochemical stability and appreciable ionic conductivity.

In this context, the aim of the present Master Degree Thesis is to develop and characterize a new NASICON composition, based on the LAGP (Lithium Aluminum Germanium Phosphate) glass ceramic electrolyte material. The addition of silica and magnesium into the LAGP structure was proposed, thus producing the glass composition $Li_{1.5}(Al_{0.3}Mg_{0.1})Ge_{1.6}(P_{2.9}Si_{0.1})O_{12}$ (LAMGPS). The effects of dopants were investigated, which could lead to a better chemical stability and higher ion mobility. More in details, starting from properly selected reactants, samples having two different glass compositions (LAMGPS and LAMGPS10) were produced through a melt-quenching synthesis method. The produced glasses were physicochemically and thermally characterized by Differential Thermal Analysis (DTA) and Heating Stage Microscopy (HSM) to assess their sinter-crystallization behavior. Bulk samples and uniaxial pressed powders samples were successively divitrified and sinter-crystallized, respectively, with proper heat treatments, to produce glass ceramics form the parent glass. X-ray Diffraction (XRD) analysis allowed to study the chemical composition and crystal structure of the samples, thus understanding which phases were present. Scanning Electron Microscope (SEM) was used to understand the morphology of the glass-ceramic samples, their densification and their conductivity. To determine the ionic conductivity of gold-sputtered samples, Electrochemical Impedance Spectroscopy (EIS) was carried out. Through the Ohm's Law, ionic conductivity reached values in the order of 10^{-5} S cm^{-1} at 20 °C. Overall, although the proposed solid state electrolyte did not reach outstandingly high ionic conductivity values, its performances are consistent. Moreover, the excess of Li in LAMGPS10 allowed to enhance the ionic conductivity, similar to analogous results in the literature for LAGP-type electrolytes.

Summarizing, even if further trials have to be addressed to promote the SSBs in the electrochemical energy storage market. The proposed synthetic route is simple and efficient, and the comprehensive characterization could shed light in the understanding of the relationship between the processing, the structure and the properties of glass ceramic solid-state electrolytes, an utmost important and up-to-date area of solid-state battery research.

Table of Contents

List of Tables

List of Figures

Acronyms

A-CAES Adiabatic Compressed-Air Energy Storage

AC Alternating Current

ASW Anodic Stability Window

CPE Constant Phase Element

CPEs Composite Polymer Electrolytes

CSW Cathodic Stability Window

DEC Diethyl Carbonate

DMC Dimethyl Carbonate

DTA Differential Thermal Analysis

EC Ethylene Carbonate

EIS Electrochemical Impedance Spectroscopy

EV Electric Vehicle

GHG Greenhouse Gases

HSM Hot Stage Microscope

ICE Internal Combustion Engine

IEA International Energy Agency

IRENA International Renewable Energy Agency

LAGP Lithium Aluminium Germanium Phosphate

LAMGPS $Li_{1.5}(Al_{0.3}Mg_{0.1})Ge_{1.6}(P_{2.9}Si_{0.1})O_{12}$

LAMGPS10 LAMGPS with 10% excess of Li_2CO_3

LATP Lithium Aluminium Titanium Phosphate

LIB Lithium Ion Battery

LISICON Lithium Super Ionic Conductor

LYB Li_3YBr_6

LYC Li_3YCl_6

NASICON Sodium Super Ionic Conductor

NIB Sodium Ion Battery

PAN Polyacrylonitrile

PC Propylene Carbonate

PEO Poly(ethylene oxide)

PHES Pumped Hydro Energy Storage

PMMA Poly(methyl methacrylate)

PVA Poly(vinyl alcohol)

PVDF Poly(vinylidene fluoride)

PVP Polyvinylpyrrolidone

RES Renewable Energy Source

RT Room Temperature

SEM Scanning Electron Microscope

SIE Solid Inorganic Electrolyte

SPE Solid Polymer Electrolyte
SSB Solid-state-battery
TES Thermal Energy Storage
WEO World Energy Outlook
WiS Water-in-Salt electrolyte
XRD X-Ray Diffraction

Chapter 1

Introduction

Electrical energy is an indispensable and effective energy vector to maintain the global standard of living. About of 65% of this energy is produced from fossil fuels, which leads to abundant greenhouse gases emissions (GHG) to the environment. Moreover, reputable institutions like International Energy Agency (IEA), International Renewable Energy Agency (IRENA) and others indicate that fossil fuels are expected to dominate the primary energy sources for many years, the global energy consumption, and consequently the global warming, continuously increases, with a growth in demand up to 28% in 2040. Consequently, to safeguard the environment, new sources of electricity production are required, in order to make a rapid and global decarbonization process.

In this process of decarbonizing the energy economy, the continuous search for new sources of electricity production has led to the progressive development of the Renewable Energy Sources (RESs), such as wind and solar and others. So, the production of energy vectors, such as hydrogen and synthetic fuels, from RESs is regarded as the best solution to the current environmental problems and large demand for fuels. Following this purpose, a deployment of renewable energy policies has been set up; thanks to the growing maturity of RESs, these policies are integrating into overall energy sector planning [1]. Moreover, the Covid-19 pandemic has caused more disruption to the energy sector than any other recent event. IEA has evaluated a reduction of 5% in energy demand, and a reduction of energy-related CO_2 emissions equal to 7%. All these data suggest a change in energy production, in which renewables prove resilient and flourish in the post-pandemic recovery, meeting 80% of global electricity demand growth during the next decade.

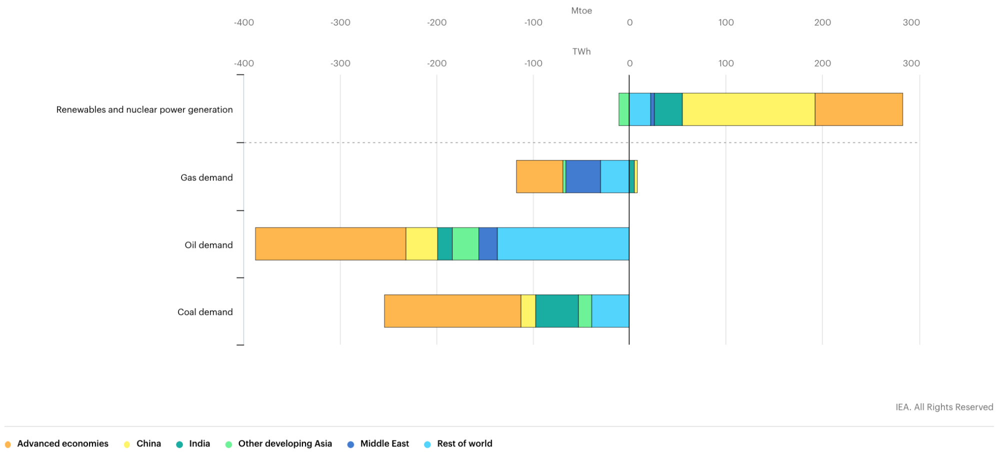

Figure 1.1: Change in power generation, 2019-2020 [2].

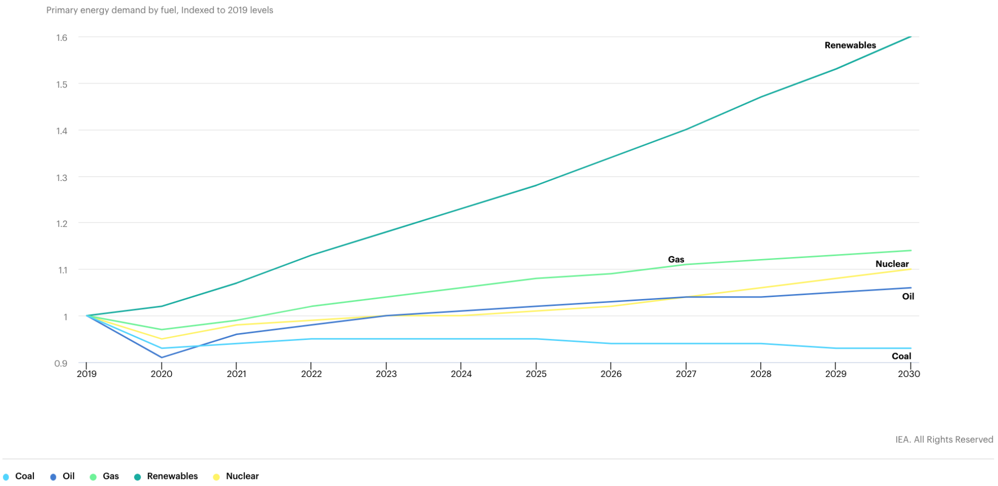

Figure 1.2: 2019-2030 trends scenario [2].

However, although the positive and encouraging projections that are underlined in the *World Energy Outlook 2020* (WEO) [2], it is still a long way up towards a sustainable development that might effectively solve the problems related to environmental pollution and global warming. In this context, the projections of CO_2 emissions are very critical, since they have expected to rebound at the end of 2021, to exceed the pre-crisis levels in 2027 and to reach the value of 36 Gt (gigatons) in 2030, thus going so far from climate goals, as accorded in the Paris Agreement.

Despite the remarkable progress in recent years, renewables are yet to reach their full potential since key barriers are present related to technology, awareness and capacity, costs, which inhibit a complete development of a so-called Green Economy. In order to achieve a better energy conversion as possible, the concept of energy storage is progressing, since it could lead to decouple power generation and load, thus assuring stability and reliability of the electrical grid. Indeed, the electrical system equipped with energy storage should allow the continuity of energy supply, thus overcoming the intermittence problem of RESs, such as wind and solar.

Following this theoretical line, many investments have made in this technology, and improved in the last decade. Figure 1.3 shows how all possible energy storage are distributed [3]. Up to 2020, installed capacities of Pumped Hydro Energy Storage (PHES) have represented the main solution. From 2025, batteries will begin to have the highest output, and will provide balance over shorter periods (hrs to days).

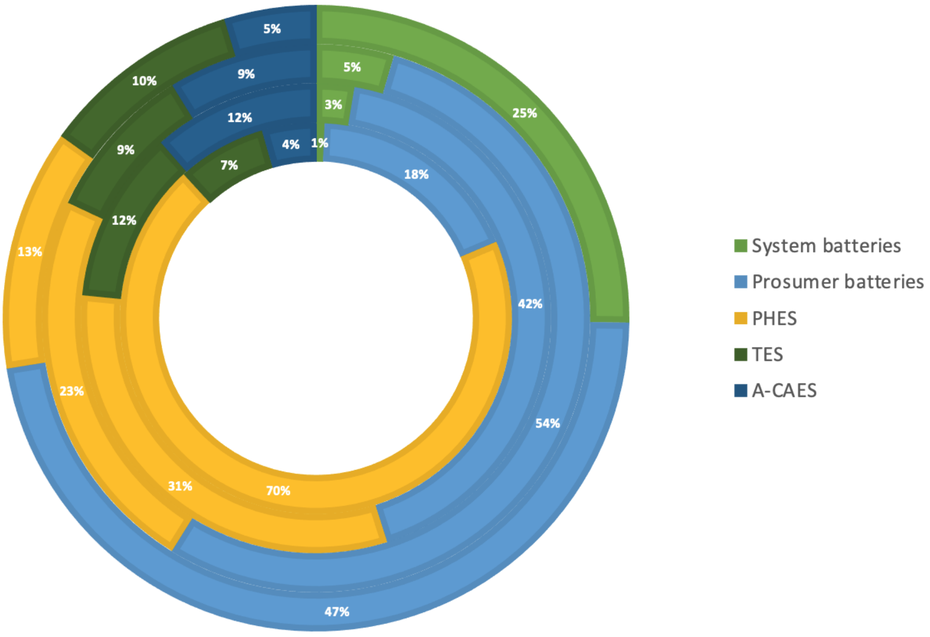

Figure 1.3: Trends scenario of energy storage technologies, 2020-2040 [3].

Also, the so-rapid electrification of the global energy supply system is involving the transportation sector. Although the Covid-19 pandemic has significantly slowed the economic development, electric mobility has accelerated, further boosted by the construction of bike lanes and other measures to promote mobility and the development of electric vehicles (EVs) [4], thus reducing the usage of internal combustion engine (ICE) cars, which abundantly participate in CO_2 emissions and overall global warming. The electrification of the sector is underlined by the growth of the sold electric cars, represented in the figure 1.4.

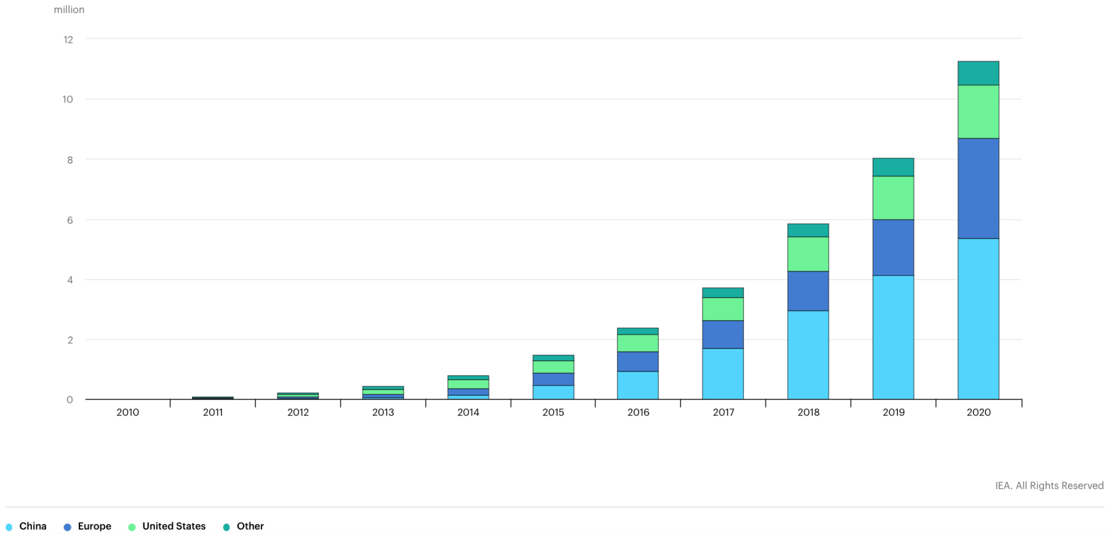

Figure 1.4: Electric vehicle stock by region in the period 2010-2020 [4].

Batteries represent a great solution in terms of service life, pollution-free operation, and overall efficiency. These factors made it possible to produce several battery systems, like Li-ion batteries (LIBs) and Na-ion batteries (NIBs).

In addition, the relevance of portable electronic devices has increased constantly in the lasts years leading to a growing interest in more efficient portable power sources, together to automotive applications, according to Fig. 1.5 [5].

However, many of above-mentioned factors are still too expensive, and they necessitate major improvements regarding performance, reliability, and materials availability and stability [6].

So, developing new electrode materials becomes important, since this can lead to

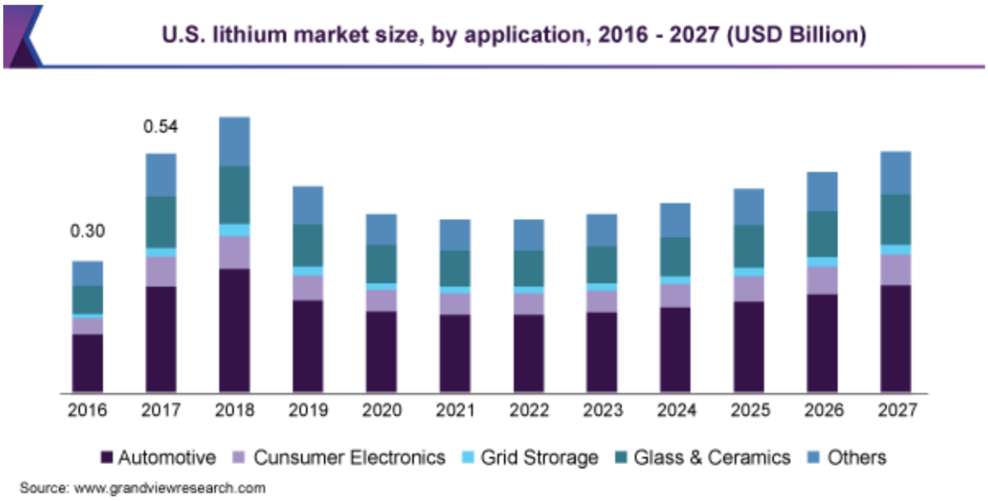

Figure 1.5: U.S. lithium market size [5].

achieve high overall performance, considering also the battery life and safety.

Chapter 2

Literature review

2.1 Electrochemical energy storage

A battery is a closed electrochemical device capable of delivering electrical energy, using the chemical energy contained in the materials constituting the electrodes, and vice versa. The operating working principle is based on three steps [6]:

1. Ionization of charge.
2. Transport of charged species.
3. Recombining of charge.

Based on that, the fundamental idea that an electrochemical energy storage device follows is the reciprocity between converting the chemical energy of fuels into electrical energy [6]. The driving force is the Gibbs free energy, indicated with ΔG, of species which participate at the chemical reaction,

$$A + B = C, \tag{2.1}$$

with ΔG measured in $\mathrm{kJ\,mol^{-1}}$. Since these are electrically charged, the energy transported by an electron is given by:

$$\Delta G = -zEF, \tag{2.2}$$

where [6]:

- F is Faraday's constant, whose value is 96,485 $\mathrm{C\,mol^{-1}}$.
- z is the charge number of the transporting species.
- E is the cell voltage.

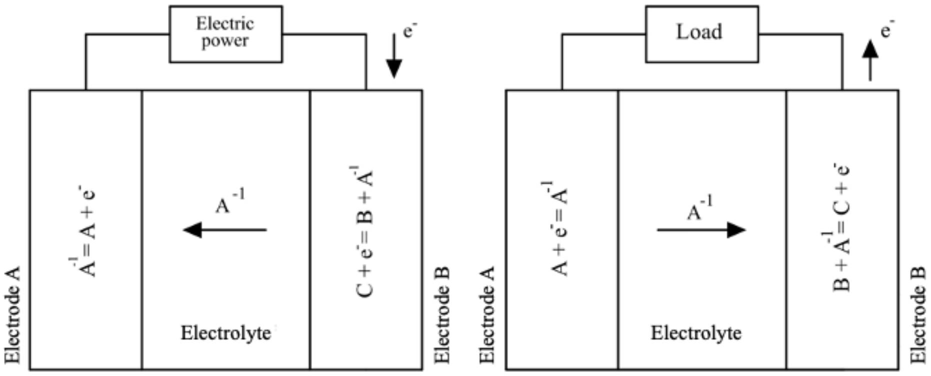

Figure 2.1: Operating principle of a battery.

The parameters that guide the innovative progress of batteries are the specific energy and specific power, which are the amount of stored electrical energy and the rate at which the energy can be extracted, respectively. They are function of the voltage of the cell, measured in volts, and capacity, measured in $\mathrm{A\,h\,kg^{-1}}$. Both are also related to the thermodynamic and kinetic constraints imposed by chemistry and materials choice. Since it is a closed system, there is no mass exchange with the environment, and the materials which participate to the electrochemical reactions are the same materials that constitute the electrodes.
This system is characterized by a connection of several cells. Each cell is constituted by three components:

- Anode, the negative electrode.
- Cathode, the positive electrode.
- The electrolyte system.

This kind of conversion occurs thanks to the reactions that happen in the electrodes, which are of reduction-oxidation type. During the chemical process, an exchange of electrons is carried out by the electro-active species in the two electrodes. When the system is connected to an external circuit, electrons start to flow from the anode, in which oxidation reaction occurs, to the cathode, in which reduction reaction occurs. To complete the circuit, the electrolyte allows to have a medium for the transfer of ions. It serves as an intermediate between anode and cathode and also as separating medium to avoid a short circuit [7].

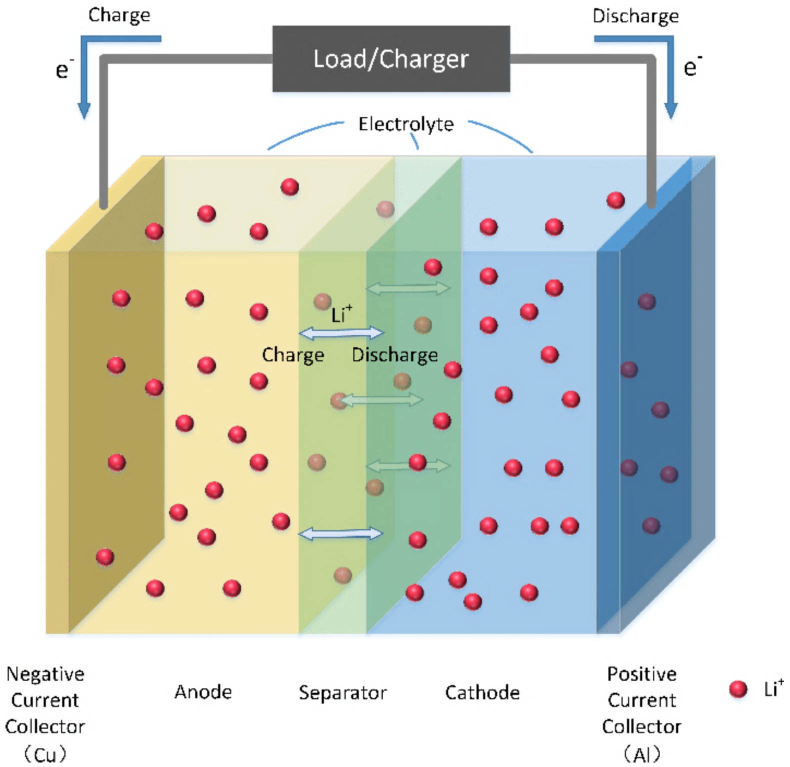

Figure 2.2: Schematic illustration of a single cell.

2.2 Li-ion batteries

Off all metals available in nature and for battery chemistry, lithium (Li) is the best choice, since it is largely available until today and non toxic. Moreover, this metal is the most electropositive element in nature, with a redox potential equal to -3.04

V, and it is the lightest among all metals too, which entails having a high energy density [6, 8].

Lithium-ion batteries are electrochemical series connected cells characterized by lithium conducting electrolytes and insertion electrodes, of which the most used are graphite as anode and mixed oxides of Ni, Mn and Co as cathode. The total occurring reaction is [9]:

$$C_6Li_x + Li_{1-x}MO_2 \underset{\text{re-charge}}{\overset{discharge}{\rightleftharpoons}} 6C + LiMO_2 \tag{2.3}$$

where:

- M is a generic metal, whose choice affects the thermodynamic behaviour.
- x is amount of sites in which Li-ions can be intercalated in anode structure.

In a Li-ion battery, the Li^+ ions are transported to and from the positive or negative electrode by oxidizing metal M during charge or by reducing metal M during discharge, respectively.

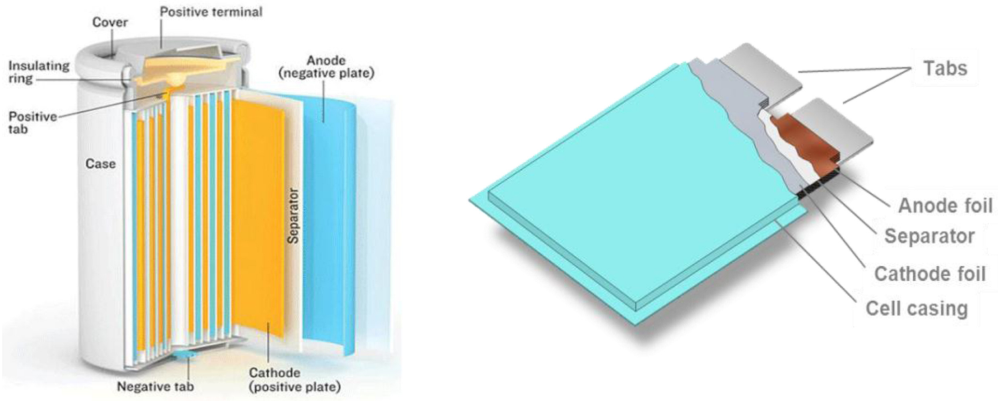

Figure 2.3: Li-ion battery cell configurations [8].

2.2.1 Discharging phase: ΔG<0 → Release of power

During this phase, in a charged battery in open circuit conditions, lithium ions are intercalated in the anode structure are in equilibrium with the ions in the electrolyte layer. As the circuit is closed, the $Li \leftrightarrow Li^+$ equilibrium is broken. So, lithium ions start travelling from anode to cathode, producing the discharging process. During it, since the lithium concentration in anode structure varies, $\Delta\mathrm{G}_{an-cath}$ will be modified, and it will decrease until it is no more able to drive battery operation.

$$anode : C_6Li_x \rightarrow 6C + xLi^+ + xe^- \tag{2.4}$$

$$cathode : Li_{1-x}MO_2 + xLi^+ + xe^- \rightarrow LiMO_2 \tag{2.5}$$

2.2.2 Re-charging phase: ΔG>0 → Absorption of power

In the re-charging process, the functioning is inverted with respect to the discharging configuration. As the circuit is closed, lithium concentration in the anode structure will involve a consequent modification of $\Delta\mathrm{G}_{an-cath}$. In particular, Gibbs free energy will grow until it reaches the value associated to the full charge state.

$$anode : LiMO_2 \rightarrow Li_{1-x}MO_2 + xLi^+ + xe^- \tag{2.6}$$

$$cathode : 6C + xLi^+ + xe^- \rightarrow C_6Li_x \tag{2.7}$$

2.3 Na-ion batteries

The continuous increasing demand of Li-ion batteries for its applications, like portable electronics and electric vehicles, is putting a strain on lithium resources of the Earth. Consequently, an influence on cost and source of the Li is expected [10]. Moreover, one of the biggest problem of Li-based batteries is the recycling, and it is yet properly an unsolved challenge [6].

Among all different possibilities, other electropositive materials such as sodium, potassium, calcium, and magnesium are quite abundant in nature. Na represents one of the best solutions: it is the second lightest alkali metal and has a slightly less reducing potential of -2.7 V, with respect to lithium one. So, sodium presents itself as a good compromise. However, due to its larger ionic radius and mass, equal to 1.06 $\mathring{A}$ and 23 $\mathrm{g\,mol^{-1}}$ respectively, developing high Na-batteries performances becomes a very hard task, since they influence interphase formation, phase stability, and transport properties [10]. This challenge can be solved with an adequate choice of materials.

The working principle of a Na-ion battery is identical with respect to Li-ion one. During the charging phase, Na^+ goes from cathode to anode through the electrolyte, and vice versa during the discharge phase.

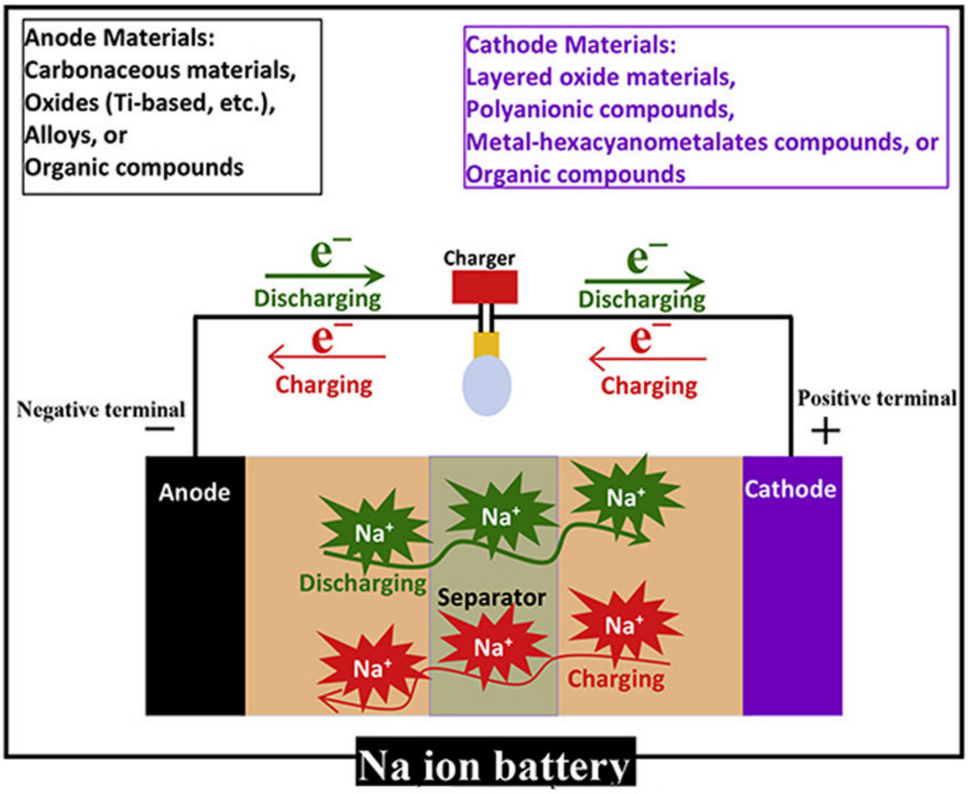

Figure 2.4: Schematic illustration of Na-ion battery [10].

2.4 Electrolytes for Li-ion and Na-ion batteries

Anode and cathode are with no doubts key elements for the working operation of a battery, and electrolyte too. In fact, it has the task of transporting ion charges. So, in terms of chemical stability, it is easy to understand that the choice of an adequate electrolyte becomes very important.

By that logic, an ideal electrolyte must satisfy these criteria [11]:

- It should be good ionic conductor and electronic insulator.
- It should have a wide electrochemical window.
- It should be inert to other components that constitute the cell.
- It should be thermodynamically stable.
- It should present low toxicity.

2.4.1 Li-based battery electrolytes

Non-aqueous organic solutions

Several kind of materials and mixture thereof have been employed as electrolyte for Li-ion applications. The most common solution consists in an electrolyte system in which one or more lithium salts are dissolved in a mixture of non-aqueous organic solvents [12]. The most used salts are lithium hexafluorophosphate $LiPF_6$ and lithium tetrafluoroborate $LiBF_4$, which are dissolved in solvents that mostly are linear or cyclic esters and ethers, such as ethylene carbonate (EC), propylene carbonate (PC), diethyl carbonate (DEC), or dimethyl carbonate (DMC). Usually, a combination of them is used in order to improve performance [13]. The salt used in commercial batteries is $LiPF_6$, which has a very good ionic conductivity, equal to $10^{-3}\ \mathrm{S\,cm^{-1}}$. However, stability problems can arise due to the high potential working [6]; in addition, it is low thermally stable, because it tends to decompose in LiF and PF_5, even in room temperature. Phosphorus pentafluoride PF_5 is a Lewis acid, which, reacting with EC and in presence of humidity, forms the hydrogen fluoride HF, that is a very dangerous gas [12]. Due to these reasons, the reliability of this technology is limited.

Aqueous electrolytes

Another possible solution is represented by the use of aqueous electrolytes, which are low cost and environmentally friendly and offer high ionic conductivity. Historically, the water use as electrolyte as electrolyte was excluded. However, lithium hydroxide LiOH is soluble in water: once lithium is intercalated in a host and presents a good potential, the reaction which forms LiOH and hydrogen does not occur. It was demonstrated by Wu Li et al. [14] that compounds unstable in water can be stable in concentrated LiOH solution. So, the potential of ions can increase and aqueous electrolytes can be considered. Also lithium salts like lithium nitrate $LiNO_3$ and lithium sulfate Li_3SO_4 are employed in aqueous solvents, as studied by Zhao et al. [15] and Luo et al. [16], with good results. Nevertheless, water has a narrow electrochemical stability window, equal to 1.23 V, which restricts a full implementation of this solution [6].

2.4.2 Na-based battery electrolytes

Despite several studies have been conducted to identify an optimal electrolyte for Na-ion batteries, a standard well performing electrolyte has not been discovered. The most widely used ones are similar to those implemented in Li-ion batteries.

Non-aqueous organic electrolytes

Most of liquid electrolytes are composed of a sodium salt, such as $NaClO_4$, Na_2SO_4, and $NaPF_6$, combined with organic solvent mixtures of linear or cyclic carbonates and ethers. Since $NaClO_4$ presents an explosive character, the use of sodium hexafluorophosphate $NaPF_6$ in carbonate-based electrolytes is preferred, whose purity influences the overall performance [17]. In addition, parasitic reactions, referable to impurities and salt decomposition, can be observed. Regarding solvent systems, the most used carbonates are similar to those employed in Li-ion batteries: propylene carbonate (PC), ethylene carbonate (EC), dimethyl carbonate (DMC), or dimethyl ether (DME), often used in mixtures. The choice of EC:DME combination represents the best solution because of its high conductivity [10]. However, it has been demonstrated that the usage of linear carbonates can lead to a detrimental effect to the battery, especially in high temperature applications [17].

Aqueous electrolytes

Aqueous NIBs represent a good solution in terms of safety, environmental friendliness and costs [17]. However, as LIB systems, Na^+ ions combined with water may lead to problems related to decomposition of electrolyte and instability of electrodes due to reactions between them and water or O_2 [18]. Despite of this, Young et al. [19] have demonstrated a possible configuration of $NaTi_2(PO_4)_3/Na_{0.44}MnO_2$ cells, with excellent performances.
Another possible solution is represented by "water-in-salt" (WiS) electrolytes, constituted by concentrated solutions of salt [17], in which the average number of H_2O molecules is far below the "solvation number" [20], that is the average number of water molecules bound more strongly to the solute than are bound to others [21]. This can lead to high value of conductivity and an enhancement of electrochemical stability window of the aqueous electrolytes up to almost 3 V [17].

Chapter 3

A new trend of innovation: solid-state batteries

In the last 200 years, the usage of batteries with liquid solution as electrolyte has represented the principal solution, since they are low cost and easy to prepare. The continuous increasing demand of electronic devices, electric vehicles and grid-energy storage, with the latter useful for electricity produced by intermittent renewable sources, has lead to a research in new possible solutions, since the available commercial batteries do not satisfy the demands of above-mentioned items [22]. Though organic liquid electrolytes present several advantages such as high ionic conductivity, maximizing the electrolyte-electrode contact area and minimizing the electric resistance between them, they suffer from low chemical and thermal stability, and low Li^+ ion transference number. Moreover, from a safety and environmental point of view, organic electrolytes incur safety issues, because of the risk of explosion and pollution [23, 24].

Today, researchers are focused on solid-state batteries (SSBs), based on a solid electrolyte. In contrast to liquid electrolytes, the solid ones can offer an enhanced safety, increased energy and power density, which can expand the operation temperature range, and improve cycling stability and lifetime [25]. Furthermore, solid-state batteries can be stacked in a single package, thus removing the possibility of an ionic short circuit. Such a configuration permits to reduce the dead space between single cells, and so the weight and volume of the package [26].

The history of solid ionic conductors starts from the 19-th century, when Faraday discovered a high conduction in heated solid Ag_2 and PbF_2 [22]. After a stalemate, from the 1960s the topic about solid-state electrolytes was resumed.

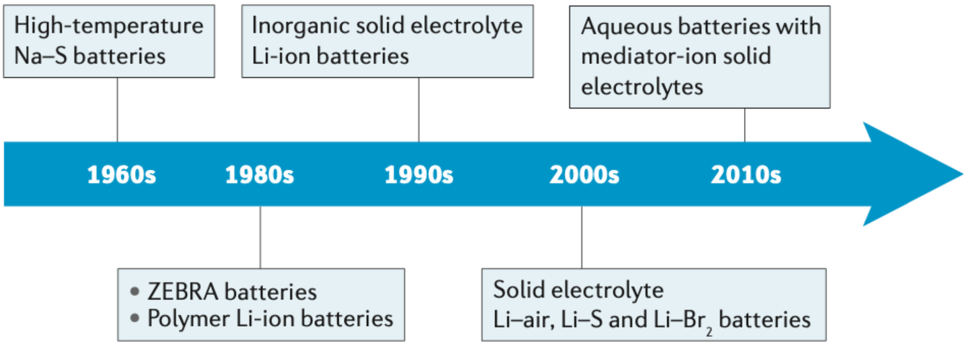

Figure 3.1: Timeline of development of solid-state electrolytes [22].

Starting from that, an ideal solid electrolyte is expected to have [25]:

- Fast ion dynamics and negligible electronic conductivity.
- Wide electrochemical potential window.
- Good mechanical properties.
- Great thermal stability.
- Low cost synthesis process.

Upon battery cycling, ions travel from the electrodes through the electrolyte. Since any impedance present in an equivalent electric circuit causes a loss of charge, having a high ionic conductivity becomes essential [27].
Ionic conduction is driven by a diffusion mechanism and by electrochemical potential gradients in the system. Following the Nernst-Planck equation, which correlates the flux of charged species to chemical and electrochemical gradient, ∇c_i and $\nabla \varphi$, respectively, it is possible to determinate the current density j [28]:

$$j = -F^2 \nabla \varphi \sum_i \mu_i c_i - F \sum_i D_i \nabla c_i + F\mathbf{u} \sum_i c_i \tag{3.1}$$

Here, F is the Faraday constant, μ_i is the mobility of charged species i, c_i is the concentration of dissociated ion pairs, D_i is the diffusion coefficient, and $\mathbf{u}$ is the convective velocity of the medium where there is the transport of ions. Considering a solid state electrolyte, the velocity and the concentration gradient can be negligible. Therefore, the conductivity can be obtained following the equation 3.2:

$$\sigma = -\frac{j}{\nabla \varphi} = F^2 \sum_i \mu_i c_i \tag{3.2}$$

where the mobility is related to the diffusion coefficient through the equation 3.3:

$$\mu_i = \frac{D_i}{k_B T} \tag{3.3}$$

Therefore, the transport of ions is a consequence of microscopic ion diffusion, described by ion hopping. The probability of a successful jump, through which an ion moves from one stable site to an adjacent one is expressed by the equation 3.4 [27]:

$$p = \exp\left(-\frac{\Delta G_m}{k_B T}\right) \tag{3.4}$$

Here, ΔG_m is the Gibbs free energy difference between the stable point and adjacent one, k_B is the Boltzmann constant, and T is the absolute temperature. A random-walk diffusion coefficient D_i is given by 3.5:

$$D_i = \gamma a_0^2 f_0 \exp\left(-\frac{\Delta G_m}{k_B T}\right) \tag{3.5}$$

where γ is the geometric factor, a_0^2 is the hopping distance and f_0 is the frequency for ion hopping. The velocity at which ions propagate is given by:

$$v_m = \left(\frac{\nu Z e a_0^2 E_v}{k_B T}\right) \exp\left(-\frac{\Delta G_m}{k_B T}\right) \tag{3.6}$$

Z is the charge number of mobile ion, e is the electron charge, a_0 is the jump distance, E_v is the applied potential, and ν is the attempt frequency. Combining equation 3.2 and equation 3.5, the conductivity can be written as:

$$\sigma_{ion} = \left(\frac{\gamma c \nu Z^2 e^2 a_0^2}{k_B T}\right) \exp\left(-\frac{\Delta G_m}{k_B T}\right) \tag{3.7}$$

Since the Gibbs free energy is function of enthalpy and entropy, it must be separated, in which the entropy contribution is negligible. So, writing the pre-exponential factor as σ_0, the conductivity formula definitely becomes:

$$\sigma_{ion} = \frac{\sigma_0}{T} \exp\left(-\frac{\Delta H_m}{k_B T}\right), \tag{3.8}$$

The migration enthalpy is often generalized with the activation energy E_a, measured in $\mathrm{kJ\,mol^{-1}}$ or eV. Finally, the well-known Arrhenius equation is obtained:

$$\sigma_{ion} = \frac{\sigma_0}{T} \exp\left(-\frac{E_a}{k_B T}\right), \tag{3.9}$$

Based on conductivity equation, in order to have a fast ion transport, different requirements can be formulated:

- A high dimensionality of the conduction pathways.
- A high carrier density c.
- A low value of activation energy E_a.

From the above-mentioned conditions, some structural and engineering requirements are needed, which are: 1) a polyhedral connectivity that allows for lower energy jumps between sites; 2) structural changes of anions and cations with different ionic radii, which permit to modify diffusion pathways and activation energy, consequently; 3) creation of empty sites through aliovalent substitution that increases the charge carrier density.

Certain classes of solid electrolytes are able to reach ionic conductivity values at room temperature (RT) that can be comparable to those of liquid electrolytes [28]. Considering the above-mentioned characteristics, different classes of solid electrolytes can be classified [22, 29]:

1. Hydride-based electrolytes.
2. Halide-based electrolytes.
3. Thin-film electrolytes.
4. Solid polymer electrolytes (SPEs).

5. Composite polymer electrolytes (CPEs).
6. Solid inorganic electrolytes (SIEs), that can have a ceramic or a glass-ceramic structure.

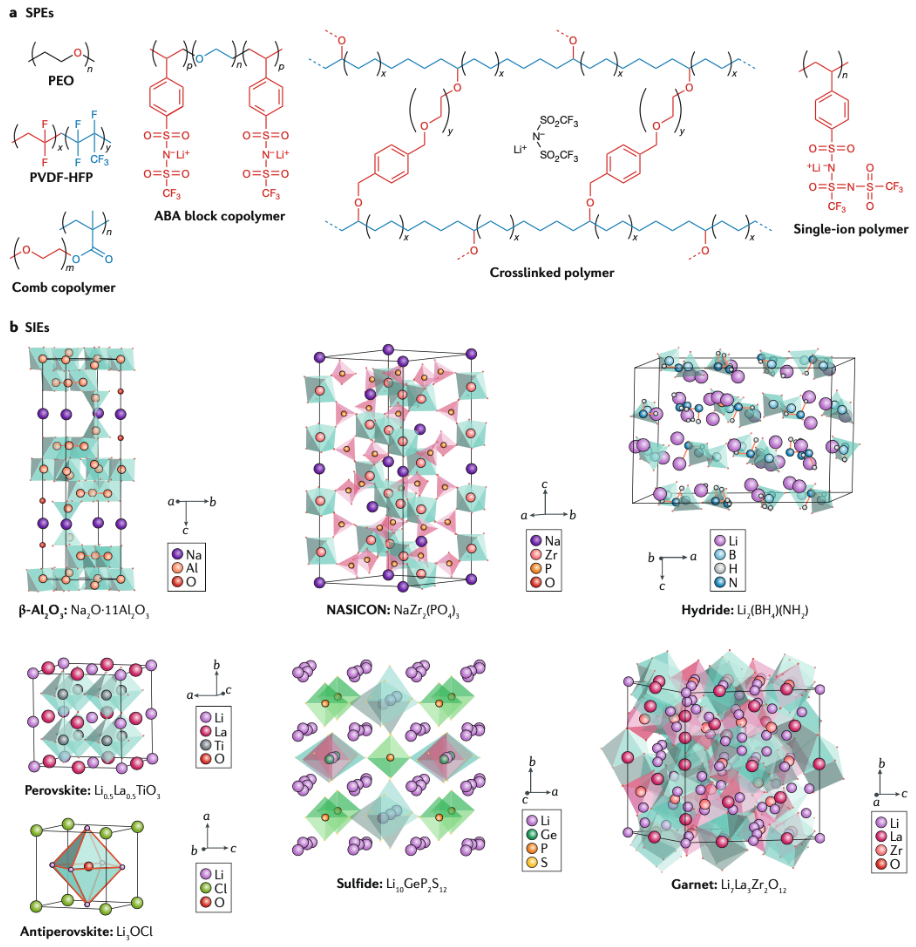

Figure 3.2: Structure of: a) SPE electrolytes, b) SIE electrolytes [28].

3.1 Hydride-based electrolytes

The general hydride structure consists of a metal cation and a complex anion, expressed by the formula M(M'H_n), in which cations can be Li^+, Na^+, Mg^{2+}, while anions can be $[BH_4]^-$, $[NH_2]^-$, $[AlH_4]^-$, and so on [30]. Hydride-based systems have been suggested as promising electrolytes for all-solid-state batteries. In fact, the study performed by Matsuo et al. [31], lithium borohydride $LiBH_4$, constituted by ionic bonding between Li^+ and $[BH_4]^-$, has shown a low conductivity in the low temperature (LT) phase, in the order of 10^{-8} and 10^{-6} $S\,cm^{-1}$. However, with the increasing of temperature, the value of conductivity increased up to 10^{-3}, due to the fast lithium ionic motion. Consequently, numerous studies on solid electrolytes based on hydrides have been carried out, that can be exhibit fast Li-, and also Na-ionic conductions. However, these electrolytes can encounter any issues regarding compatibility with cathode materials.

3.1.1 Fast Li-ionic conductors

Based on high conductivity of $LiBH_4$, many systems have been studied, in the form $LiBH_4$-LiX (X=Cl, Br and I). The substitution of $[BH_4]^-$ by iodide ions I^-, which have a larger ionic radius, improves the conductivity, that can arrive up to a value of 2 x 10^{-5} $S\,cm^{-1}$ at 300 K. Unemoto et al. [30] discovered that a system consisting of $LiBH_4$-$LiNH_2$-LiI can exhibit conductivities of 2 x 10^{-4} $S\,cm^{-1}$. This suggests that systems based on $LiNH_2$-LiI can reach similar values [32].
Also systems consisting of Li-alanates, $LiAlH_4$, Li_3AlH_6 are fast ionic conductors. However, they reach lower values than the previous ones, in the range between 10^{-9} and 10^{-5} $S\,cm^{-1}$ [30].

3.1.2 Fast Na-ionic conductors

The choice of solids that present fast sodium ionic conductivity is very limited with respect to lithium one. Starting from the system $NaBH_4$-$NaNH_2$-NaI, a conductivity value of 2 x 10^{-6} $S\,cm^{-1}$ at 300 K in the solution $Na_2(BH_4)(NH_2)$ was obtained [30]. Also sodium alanates have been studied, but they are limited to conductivity values of 10^{-6} - 10^{-8} $S\,cm^{-1}$.

3.2 Halide-based electrolytes

In this kind of materials, the nature of halogen anions is exploited. In fact, they can exhibit an interesting fast Li-ion transport, since the interaction between them and lithium ions is very weak. Moreover, they present ionic radii very large, with respect to other anions like O_2^-, Cl^- or Br^-. Although these are not negligible advantages, studies on halide electrolytes are very few. Asano et al. [33] have proposed two lithium-ion-conducting halide solid electrolytes, which are Li_3YCl_6 (LYC) and Li_3YBr_6 (LYB). They observed that, by a mechanochemically synthesis, these electrolytes offered high conductivity, electrochemical stability and good mechanical properties. More precisely, ionic conductivities at room temperature were 0.51 $mS\,cm^{-1}$ for LYC and 0.72 $mS\,cm^{-1}$ for LYB.

Another study was carried out in 2008 by Maekawa et al. [34], in which Li_2ZnI_4 was used for the fabrication of the composite with pore size controlled mesoporous-Al_2O_3. However, the result was not what they expected, because the value of conductivity was very low, equal to 2.4 x 10^{-8} $S\,cm^{-1}$ at 300 K.

3.3 Thin-film electrolytes

Thanks to works conducted in Oak Ridge National Laboratory, solid-state thin-film lithium-ion batteries were developed. Electrolytes can be produced by different vapour deposition processes, such as pulsed laser deposition and chemical vapour deposition [22]. As standard electrolyte, the used material is the glassy lithium phosphorus oxynitride (LiPON). Moreover, it presents stability with lithium at potential 0-5.5 V and an ionic conductivity close to 3 x 10^{-6} $S\,cm^{-1}$ at room temperature [35].

Another serie of thin film was examined, corresponding to the use of lithium borophosphate as an alternative to LiPON. In fact, the addition of boron oxide B_2O_3 to a phosphate network can lead to an increase in ionic conductivity and chemical durability [36]. Based on that, Fleutot et al. [37] proposed radio frequency sputtering and characterization of lithium borophosphate glasses, reaching a maximum conductivity value of 1.2 x 10^{-6} $S\,cm^{-1}$ at room temperature.

3.4 Solid polymer electrolytes (SPEs)

This type of electrolytes shows several advantages, such as ease of synthesis, chemical stability, low cost, good flexibility, the latter useful to compensate the volume changes of electrodes and to improve performance and cycle life [38]. The most common polymer matrices are poly(ethylene oxide) (PEO), poly(methyl methacrylate) (PMMA), poly(vinylidene fluoride) (PVDF), poly(vinyl alcohol) (PVA), etc. PEO is the most widely used polymer due to its stability with many electrode materials and high ionic conductivity in its amorphous state. [28]. However, due to their low dielectric constants (ϵ<5), the ion-pair dissociation is not facilitated. For these polymers, the ion transport mainly occurs in the amorphous regions, where the molecular chains can oscillate above their glass transition temperature T_g. The presence of electric field can facilitate the hopping phenomenon of Li^+ or Na^+ ions, thus resulting in an enhanced ionic conductivity [29].

3.4.1 PEO-based electrolytes

A typical PEO-based electrolyte is formed by dissolving a salt, lithium or sodium salt, into a PEO matrix. So, the main requirement is represented by the choice of salt, depending on how much it dissolves in the polymer matrix [39]. The most employed lithium salts are lithium perchlorate $LiClO_4$, lithium hexafluorophosphate $LiPF_6$, lithium hexafluoroarsenate $LiAsF_6$, and lithium tetrafluoroborate $LiBF_4$. In the last years, researchers moved towards the use of imide salts, such as LiTFSI and LiFSI.

The typical value of conductivity of PEO-LiX systems is well below $10^{-4}\,\mathrm{S\,cm^{-1}}$ at room temperature. Among them, $LiCLO_4$ presents good conductivity and electrochemical stability. However, it is characterized by an unsafe use due to strong ability to oxidize. Also the PEO-based electrolyte with lithium salt $LiPF_6$ has a high ionic conductivity, equal to 1.13 x $10^{-3}\,\mathrm{S\,cm^{-1}}$, but its ease of decomposition with moisture leads to react with electrodes, bringing to formation of hydrogen fluoride HF.

Regarding sodium salts, the first used salt was sodium perchlorate $NaClO_4$, which showed an ionic conductivity of about 3 x $10^{-6}\,\mathrm{S\,cm^{-1}}$ at RT. Nowadays, the most used salts are sodium hexafluorophosphate $NaPF_6$, sodium thiocyanate NaSCN, sodium tetrafluoroborate $NaBF_4$, and sodium bis(trifluoromethanesulfonylimide) NaTFSI, beyond $NaClO_4$ [29]. Among all these sodium salts, NaTFSI salt with PEO matrix has the highest ionic conductivity, equal to 1.3 x $10^{-3}\,\mathrm{S\,cm^{-1}}$ above

80 °C. However, it has a low corrosion potential of aluminum foil.

3.4.2 Other polymer-based electrolytes

Due to low oxidation potential and poor mechanical properties, PEO is characterized by a low ionic conductivity, since it is constituted by a crystalline structure at RT, harmful to ionic conductivity. Substituting the main active group of C=O by C=N, polyacrylonitrile PAN is formed. Few studies have been carried out, especially with sodium salts. The best solution is represented by the system $NaCF_3SO_3$-PAN, in which the conductivity is equal to 7.13 x 10^{-4} S cm^{-1} at RT. Also $NaClO_{3^-}$, $NaClO_{4^-}$, and NaF with polyvinylpyrrolidone (PVP) were studied, but they did not present the desired ionic conductivities [29].

3.5 Composite polymer electrolytes (CPEs)

Starting from SPEs, several methods have been considered, in order to further increase the ionic conductivity of solid polymers. Through polymer crosslinking, copolymerization, and doping of additives, new systems have been studied, which are the composite polymer electrolytes (CPEs). They present good electrochemical properties, such as higher ionic conductivity and chemical stability, but also appreciable thermomechanical property, such as good flexibility [29].

The incorporation of ceramic fillers represents the main solution in the field of CPEs. So, ceramic-polymer composite electrolytes have been studied. The main analyzed additions were titanium dioxide TiO_2, silica SiO_2, and alumina Al_2O_3 [40]. TiO_2, added to PEO-based system with dissolved salt $NaClO_4$, showed a higher ionic conductivity of 2.62 x 10^{-4} S cm^{-1} at 60 °C, with respect to a simple solid polymer electrolyte with only the oxide, which presents an ionic conductivity equal to 1.35 x 10^{-4} S cm^{-1} [29]. A hybrid system with $NaClO_4$-PEO-5%SiO_2-x%, with x = 50, 70, for all-solid-state sodium ion batteries has showed a high conductivity, achieving a value of 1.3 x 10^{-3} S cm^{-1} [41].

Croce et al. [42] studied a PEO-$LiClO_4$ system mixed with both TiO_2 and Al_2O_3 powders, reaching conductivities of 10^{-4} S cm^{-1} at 50 °C and 10^{-5} S cm^{-1} at RT.

3.6 Solid Inorganic Electrolytes (SIEs)

The most important property that characterizes SIEs is the symmetrical skeleton structure and mobile ions [38]. As cited by Ohno et al. [27], the ion conduction is influenced by ions hopping from one site to adjacent one. Consequently, the conductivity strongly depends on the number of vacancies and energy barrier for hopping. Moreover, the value of ionic conduction can vary from bulk grains to grain boundaries within the electrolyte. Several studies have been demonstrated that the ionic conductivity can increase its value by aliovalent substitution which leads to create vacancies. In particular, it has been noticed that the conductivity usually reaches a maximum and then starts to decrease. This lowering can be caused by the occurring distortion of lattice and the increasing of migration energy [43].

SIEs are characterized by high ionic conductivities, in the order of around 10^{-4} $\mathrm{S\,cm^{-1}}$ at RT, good mechanical properties, wide electrochemical stability windows, and notable thermal stability for applications above 100 °C. However, several disadvantages can occur, such as manufacturing difficulties, poor compatibility with electrodes, and the risk of metal dendrite growth [28]. To overcome these issues, different structures have been designed, which the main solution are represented by the development of sulfide-based electrolytes and oxide-based inorganic electrolytes [38].

3.6.1 Sulfide-based solid electrolytes

From 80s, with the first system consisting of Li_2-SiS_2, sulfide electrolytes have represented an attractive choice, due to the high polarizability and large ionic radius of sulfur, which permits a fast Li/Na ion conduction, thus providing high ionic conductivities. Furthermore, they require low temperature for their synthesis [29, 38].

One of the best composition was synthetized and studied by Tatsumisago et al. [44], in which, doping Li_2-SiS_2 system with Li_3PO_4, the value of 9×10^{-4} $\mathrm{S\,cm^{-1}}$ was achieved. In the recent years, Kamaya and colleagues discovered a new sulfide, belonging to the family of $Li_{10}MP_2S_{12}$ (M = Si, Ge, Sn), with chemical formula

$Li_{10}GeP_2S_{12}$, that showed a record ionic conductivity, equal to 12 $mS\,cm^{-1}$, a value comparable to liquid electrolyte [27, 45]. Even if Kato's group has discovered a new sulfide electrolyte, i.e. $Li_{9.54}Si_{1.74}P_{1.44}S_{11.7}Cl_{0.3}$, with the highest ionic conductivity that was reported for lithium conductor applications, which is 25 $mS\,cm^{-1}$ at room temperature, this type of electrolyte has a limited electrochemical windows (1.71 V-2.15 V), which limits its application. [26, 46].

Considering Na fast ionic conductors, the most common sulfide-based electrolyte is Na_3PS_4. Hayashi et al. [47] have made a comparison between a Na_3PS_4 glass pellet and a glass-ceramic with cubic Na_3PS_4, demonstrating that the first exhibited an electrical conductivity equal to 6×10^{-6} $S\,cm^{-1}$, the latter a conductivity of 2×10^{-4} $S\,cm^{-1}$, both at RT. This large enhancement was due to cubic Na_3PS_4 and a lower value of activation energy for ion hopping equal to 27 $kJ\,mol^{-1}$. Furthermore, the wide voltage window of about 5 V is a good response. However, systems based on sulfide suffer from chemical stability, as they tend to decompose through hydrolysis in air [38]. Starting from Na_3PX_4 system, an anion substitution of S^{2-} with Se^{2-} was studied by Yang and colleagues [48]. The reasons why this substitution are due to the larger atomic radius of selenium and its higher polarizability. They were able to reach a conductivity value equal to 1.16 $mS\,cm^{-1}$, comparable to liquid electrolyte alternatives.

Moreover, starting from the success of LGPS family, a seemingly consideration was studied Na^+ conductors, with a chemical formula $Na_{10}MP_2S_{12}$ (M = Si, Ge, Sn). For each composition, the conductivities reached a value of 0.4 $mS\,cm^{-1}$ for Sn application and 2.4×10^{-5} $S\,cm^{-1}$ for Ge application, while for Si application the cationic substitution was not applicable [46, 49].

3.6.2 Oxide-based electrolytes

With respect to sulfide-based electrolytes, oxide-based electrolytes present a better chemical stability. Thus, they can be used to obtain high overall battery performance and long cycling life.

Most of them are detailed below, whereas NASICON-type, which is subjected to this study, are reported in the section 3.6.3.

Na-β/β''-Al_2O_3

This type of electrolyte is well known in Na-S and Na-metal chloride batteries, since it was the first electrolyte used for these applications. Two different crystal structure exist, which are β-Al_2O_3, hexagonal, and β''-Al_2O_3, rhombohedral. The latter presents a higher ionic conductivity, which ranges from 0.2 to 0.4 $S\,cm^{-1}$ at RT, with respect to β one [46].

Fracture of β''-alumina is one of the most important issues regarding the cell life. To remedy this, a possible solution is the incorporation of zirconium oxide ZrO_2 into the matrix, even if it reduces the electrical properties since zirconia is not a Na-ionic conductors at battery operating temperature [50]. Moreover, the elevated sintering temperature (1200-1500 °C) limits its application.

Perovskite type Li conductors

The most attractive materials is the lithium lanthanum titanate perovskite $Li_{3x}La_{2/3-x}TiO_3$ (LLTO), since it has a high bulk ionic conductivity, in the order of 10^{-3} $S\,cm^{-1}$ and a wide electrochemical window [46].

LLTO has a perovskite structure (ABO_3), where A is a rare earth and its sites are partially occupied by lithium or lanthanum, and B is a transition metal. These three elements combine together to build a cubic structure, where A sites occupy the vertex of cube, B site occupies the center of cube, while O sites occupy the center of each face [9]. So, it is easy to understand that the Li^+ conductivity strongly depends on structural disorder and chemical composition of A-site. Furthermore, LLTO suffers from large boundary resistance [51]. In conclusion, more in depth studies are required for the fully application on all-solid-state lithium-ion batteries.

Garnet-type Li conductors

These oxides derive from ideal garnet structure with formula $A_3B_2(XO_4)_3$, where A-sites are antiprimastic, B-sites are octahedral, and X-sites are tetrahedral. In lithium garnets, Li^+ ions occupy the tetrahedral sites [43]. To enhance the ionic conduction, it is necessary to increase the lithium content. The most known garnet-type electrolyte is $Li_7La_3Zr_2O_{12}$ (LLZO), which is able to reach a conductivity of 0.3 $mS\,cm^{-1}$ at 25 °C. Moreover, it has a wide potential window [46]. The main challenge regards its stability against lithium metal, which leads to several studies on Li/LLZO interface, with ideally minimal pore or dendrite formation. A possible solution can be the application of alloying interlayers, but more researches are needed to find a optimal process [27].

LISICON type electrolytes

The name LISICON derives from LIthium Super Ionic CONductor, following the initial composition $Li_{14}Zn(GeO_4)_4$. The structure is very similar to Li_3PO_4 one, in which oxygen atoms are thought as a distorded hexagonal close packing, while cations are arranged in a tetrahedral coordination. Lithium ions that are located in LiO_4 tetrahedra diffuse between them and interstitial sites located in the PO_4 polyhedra [27, 43].

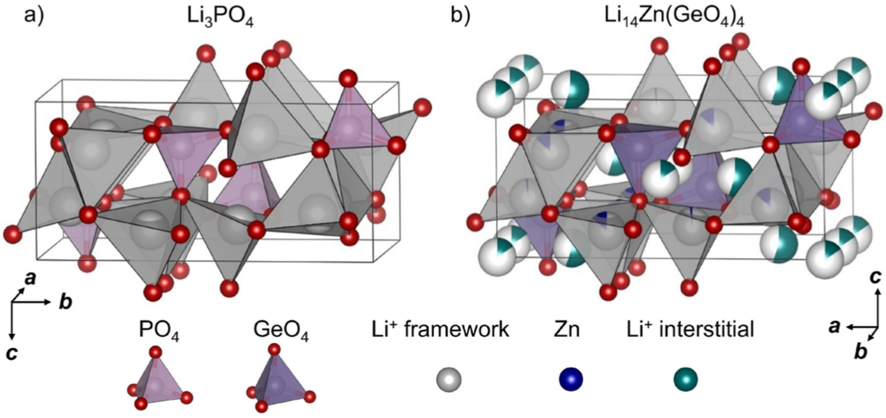

Figure 3.3: Structure representation of: a) Li_3PO_4 and b) $Li_{14}Zn(GeO_4)_4$ [27].

Several studies on LISICON family have been conducted, starting from the general formula $Li_xM_xO_4$. In the case of $Li_{2x}Zn_{2-x}GeO_4$, zinc atoms are placed in lithium positions, while germanium atoms in P positions. As the value of x increases, Li^+ ions occupy the octahedral sites, which lead to an enhancement of ionic conductivity. Good results have been obtained with the solid solutions of Li_3XO_4 (X=P, V, As) and Li_4MO_4 (M=Si, Ge, Ti), with general formula $Li_{3+x}X_{1-x}M_xO_4$. The studies have observed that the maximum values of conductivity, in the range of 10^{-6}-10^{-5} S cm^{-1}, are obtained when x assumes intermediate values, probably due to the generation of high concentration of ions. In 2019, Zhao and colleagues [52] experimented the possibility of a polyanionic doping. Varying x in the general formula $Li_{3.75-0.75x}(Ge_{0.75}P_{0.25})_{1-x}V_xO_4$, they obtained the best result in the system $Li_{3.53}(Ge_{0.75}P_{0.25})_{0.7}V_{0.3}O_4$, that showed a bulk ionic conductivity equal to 5.1 x 10^{-5} $\mathrm{S\,cm^{-1}}$.

Generally speaking, the main questions regarding Li-ion transport are several, including the carrier density, Li^+ mobility, and so on. However, studies more detailed on LISICON family and how lithium ion transport works are required, since the articles in literature are very few, at present.

3.6.3 NASICON type electrolytes

During the last years, several researches have been carried out on the solid electrolytes with a NASICON (Na super ionic conductor) structure, which allows for a desirable ionic conductivity due to the mobile Na/Li ions [53].

The first study on NASICON structure was conducted by Hong in 1976, who focused on searching new possible skeleton structures for fast ion transport. Consequently, the system with the general formula $Na_{1+x}Zr_2Si_xP_{3-x}O_{12}$ was prepared [54].

The general formula of NASICON compounds is $A[M_2(PO_4)_3]$, where A and M are monovalent and tetravalent cations, respectively. This structure with space group $R\overline{3}c$ is characterized by a link between AO_6 and MO_6 octahedra, which share the oxygen atoms with PO_4 tetrahedra, organizing a 3D structure. In this way, two kinds of sites for ions are formed, in which Li ions reside, called M1 site (octahedral vacancies) and M2 site (tetrahedra vacancies). Also bottlenecks are created, where the ions can move [55, 56].

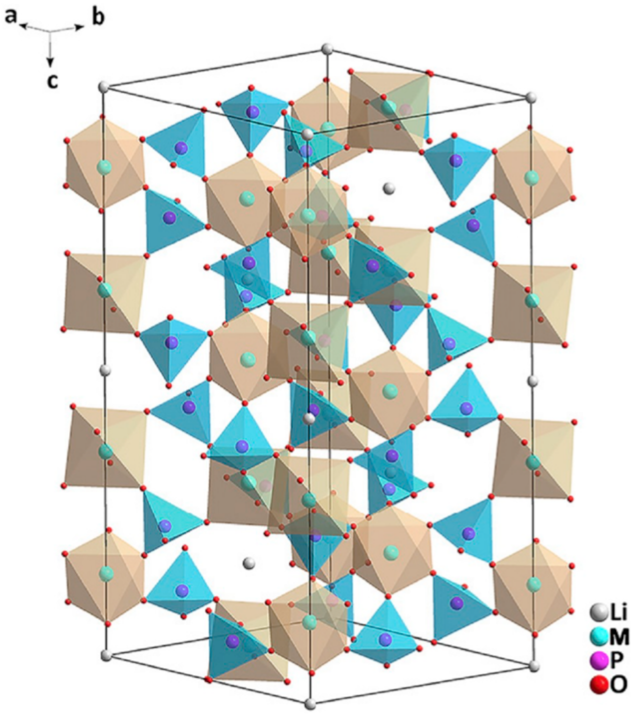

Figure 3.4: NASICON structure of $LiM_2(PO_4)_3$ [56].

Among all of the $LiM_2(PO_4)_3$ materials, those with Ti^{4+} or Ge^{4+}, generating the system LTP and LGP, are the most studied. Systems with titanium are characterized by an instability at the interface with lithium metal, since Ti^{4+} reduces into Ti^{3+}. Systems with germanium can offer a higher ionic conductivity, even if it is not very high, in the order of 10^{-6} S cm^{-1} at room temperature [57]. An enhancement of conductivity can be obtained by partial substitution of Ti^{4+}, or Ge^{4+}, by trivalent cations, since it offers a higher charge carrier number and a lower porosity of the pellets. Al^{3+}, Ga^{3+}, Cr^{3+}, Y^{3+}, Fe^{3+}, and La^{3+} are the composition already studied [27, 58]. The partial substitution of Ge^{4+} by Al^{3+} permits that extra content of lithium is introduced in M2 sites, thus maintaining the neutrality of material, and enhancing the conductivity value up to 10^{-4} S cm^{-1}. Moreover, since Al^{3+} cations are smaller than Ge^{4+} ones, the dimension of the cell is reduced, thus leading to an effect of densification, and obtaining a more accelerated ionic mobility [25, 59].

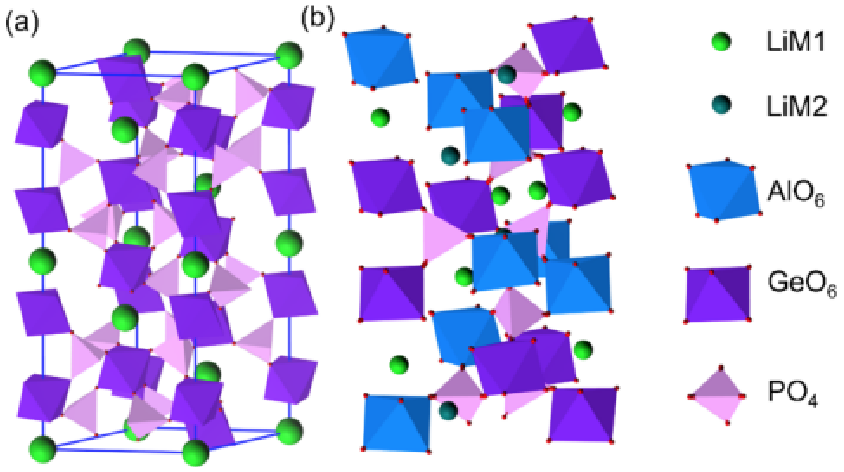

Figure 3.5: Structure representation of: a) $LiGe_2(PO_4)_3$ and b) LAGP [60].

Further advantages of LAGP (lithium aluminium germanium phosphate) glass-ceramic are to be less sensitive to reduction, compared to LATP (lithium aluminium titanium phosphate) system, the ease of synthesis, characterized by the melt-quenching method, through which the glass is formed, heat treatments for crystallization, through which the dominant NASICON structure appears [60, 61]. The secondary phase is characterized by the presence of aluminium phosphate $AlPO_4$, that is amorphous. Its quantity depends on several factors, such as synthesis and process parameters. Shin and colleagues [62] demonstrated that a little content of aluminium can enhance the conductivity. If a big quantity is present, the presence of secondary phase can easily occur. However, even if it is non conductive, the presence of $AlPO_4$ leads to a denser structure. Thus, both for LATP and LAGP, the ideal content of Al is around $x = 0.4 - 0.5$.

Starting from this criterion, and considering the $Li_{1+x}Al_xGe_{2-x}(PO_4)_3$ family, $Li_{1.5}Al_{0.5}Ge_{1.5}(PO_4)_3$ showed the best result in term of conductivity, equal to 4.2 x 10^{-3} S cm^{-1}, comparable to LATP glass ceramic ones. This composition offered superior mechanical properties, and in addition, from a electrochemical point of view, it has a good stability window (1.8-7 V vs Li^+/Li), due to the stability of Ge^{4+} towards reduction [63]. To further improve the ionic conductivity of LAGP glass-ceramic, several studies have been done, especially those based on doping solution. The effect of SiO_2 substituted in LAGP was studied by Das et al. [64], due to the fact that silica has a higher chemical stability than P_2O_5. They prepared two different glass by melt quenching method, considering two mole fraction of SiO_2: $Li_{1.5}Al_{0.5}Ge_{1.5}P_{2.9}Si_{0.1}O_{12}$ (LAGP1) and $Li_{1.5}Al_{0.5}Ge_{1.5}P_{2.5}Si_{0.5}O_{12}$ (LAGP2). From measurements, the substitution of silica influenced the formation of crystalline phases in the samples, thus leading to a change of electrical properties. LAGP1, characterized by a major crystalline phase, showed a higher conductivity, equal to 2.45 x 10^{-4} $\mathrm{S\,cm^{-1}}$, with respect to LAGP2, that showed a minor crystalline phase and, consequently, a lower conductivity, equal to 8.95 x 10^{-6} $\mathrm{S\,cm^{-1}}$. Both conductivity values were obtained at room temperature. At 373 K, they arrived to 6 x 10^{-3} $\mathrm{S\,cm^{-1}}$ and 3.1 x 10^{-4} $\mathrm{S\,cm^{-1}}$ for LAGP1 and LAGP2, respectively, suggesting an employment of LAGP1 as electrolyte for Li-SSBs.

Remarkable results have been also reported for magnesium doped LAGP. Mg^{2+} cation doping represents a good solution since it is cheaper and more abundant. Further, due to its larger ionic radius than Ge^{4+} and Al^{3+}, there is the enhancement of lithium ions concentration. With these considerations, Nikodimos' group [59] studied the composition $Li_{1+x+2y}Al_xMg_yGe_{2-x-y}(PO_4)_3$. Mg-doped $Li_{1.6}Al_{0.4}Mg_{0.1}Ge_{1.5}(PO_4)_3$, called LAMGP, showed a lower crystallization temperature, 750 °C, compared to classical LAGP, thus offering an enhancement of bulk and total ionic conductivity, equal to 7.435 x 10^{-3} $\mathrm{S\,cm^{-1}}$ and 9.13 x 10^{-4} $\mathrm{S\,cm^{-1}}$, respectively. Furthermore, it was discovered that the grain size increased and grain boundary resistance decreased, consequently. Thus, a notable densification occurred, which explains the remarkable value of conductivity.

Type	**Materials**	**Conductivity [$\mathrm{S\,cm^{-1}}$]**	**Advantages**	**Disadvantages**
Oxide	Perovskite [46, 51] Na-β/β''-Al_2O_3 [46, 50] Garnet [27, 43, 46] LISICON [27, 43, 52] NASICON [25, 27, 53–64]	10^{-6}–10^{-3}	High chemical and electrochemical stability High mechanical strength Ease of synthesis	Non-flexible Expensive large-scale production
Sulfide	$Li_{10}MP_2S_{12}$ (M = Si, Ge, Sn) [27] $Na_{10}MP_2S_{12}$ (M = Si, Ge, Sn) [46, 49] Li_2-SiS_2 with Li_3PO_4 [44]	10^{-7}–10^{-3}	High conductivity Good mechanical strength Good flexibility Low grain-boundary resistance	Low oxidation stability Poor compatibility with cathode materials
Hydride	$LiBH_4$-LiX (X=Cl, Br and I) [30, 32] $LiAlH_4$ [30] Li_3AlH_6 [30]	10^{-8}–10^{-3}	Stability with lithium Low grain-boundary resistance Good flexibility and mechanical strength	Sensitive to moisture Poor compatibility with cathode materials
Halide	Li_3YCl_6 (LYC) [33] Li_3YBr_6 (LYB) [33] Li_2ZnI_4 [34]	10^{-7}–10^{-4}	Stable with Li metal Good flexibility and mechanical strength	Low oxidation voltage Low conductivity
Thin film	LiPON [35] $Li_2O/B_2O_3/P_2O_5$ [36, 37]	10^{-6}	Stable with cathode materials and lithium metal	Expensive large-scale production
Polymer	PEO-based [29, 39–42] Non-PEO-based [29]	10^{-6}–10^{-3}	Easy to synthesize Stability with lithium Low shear modulus and good flexibility	Limited thermal stability Low oxidation voltage

Table 3.1: Summary of solid electrolyte materials. Re-arranged from [22].

Chapter 4

Experimental methods

4.1 Synthesis of $Li_{1.5}(Al_{0.3}Mg_{0.1})Ge_{1.6}(P_{2.9}Si_{0.1})O_{12}$ (LAMGPS)

This master thesis work focuses on characterizing a new composition, based on LAGP electrolyte. The idea is to substitute germanium with magnesium besides Al, since Mg has a higher ionic radius, which extends Li^+ channels for the ion transport. Moreover, since Mg has a lower oxidation status (2+ instead of 3+ of Al), for every Ge^{4+} substitution with Mg^{2+}, two Li^+ are available, which favourably contributes to ionic conductivity. With respect to the literature studies, the amount of aluminum is reduced, since a content higher than 0.3 leads to the formation of a secondary phase ($AlPO_4$). Furthermore, the role of silicon is to substitute phosphorus, which positively acts on grain boundaries.

This glass composition was prepared using a standard melt-quenching method, starting from analytical reagent-grade chemicals, which were in the form of carbonate and hydrogen phosphate of proportionate amount. Starting from the stoichiometric composition, the content in moles of each element has been reported in 100 moles. These contents allowed to evaluate the number of moles of each oxide in the glass, and consequently to determine the corresponding needed moles of precursors. Finally, the amounts of reactants required to obtain the glass had been determined, which are high purity lithium carbonate Li_2CO_3 (EMSURE ACS, 99.0%), alumina Al_2O_3 (Alfa Aesar, 99.9%), magnesium carbonate $MgCO_3$ (Riedel-de Haën, 40%), germanium dioxide GeO_2 (Aldrich, 99.99%), silica SiO_2 (Honeywell, purum p.a.), and monoammonium phosphate $(NH_4)H_2PO_4$ (Carlo Erba, 99.9%), were weighted and mixed for 24 hours, in order to prepare $Li_{1.5}(Al_{0.3}Mg_{0.1})Ge_{1.6}(P_{2.9}Si_{0.1})O_{12}$ (LAMGPS). These quantities are reported in the table 4.1.

Precursors	**# of precursors**	$\%_{mol}$
Li_2CO_3	0.0267	13.39
Al_2O_3	0.0053	2.68
$MgCO_3$	0.0036	1.79
GeO_2	0.0570	28.57
SiO_2	0.0036	1.79
$(NH_4)H_2PO_4$	0.1033	51.79

Table 4.1: Stoichiometric amounts to form 15 g of LAMGPS glass.

After thouroughly mixing, the powders were transferred into a crucible and then placed into an electric furnace for the melting step. An alumina crucible was used instead. To reach a value of temperature equal to 1.350 °C, the electric furnace follows 6 steps:

1. From room temperature (RT) to 350 °C, heating rate of 10 °C/min.
2. 30 minutes at 350 °C.
3. From 350 °C to 700 °C, heating rate of 10 °C/min.
4. 30 minutes at 700 °C.
5. From 700 °C to 1.350 °C, heating rate of 10 °C/min.
6. 2 hours at 1.350 °C.

During this process, thanks to the heat provided by the furnace, compounds were released, leaving behind the desired amounts of Li_2O, MgO and P_2O_5, which constitute the glass. The reactions are expressed through the equations 4.1, 4.2 and 4.3.

$$Li_2CO_3 + heat \rightarrow Li_2O + CO_2 \tag{4.1}$$

$$MgCO_3 + heat \rightarrow MgO + CO_2 \tag{4.2}$$

$$2(NH_4)H_2PO_4 + heat \rightarrow P_2O_5 + 2NH_3 + 3H_2O \tag{4.3}$$

The melt was quenched on a brass plate at room temperature, thus obtaining the drop shape in figure 4.1. Since the material was cooled from an elevated temperature, thermal stresses may occur, which can weaken the material or, in extreme cases, lead to fracture. To remove these stresses, an annealing heat treatment was carried out, at a temperature T_g - 10 °C. Then, the glass was slowly cooled to room temperature.

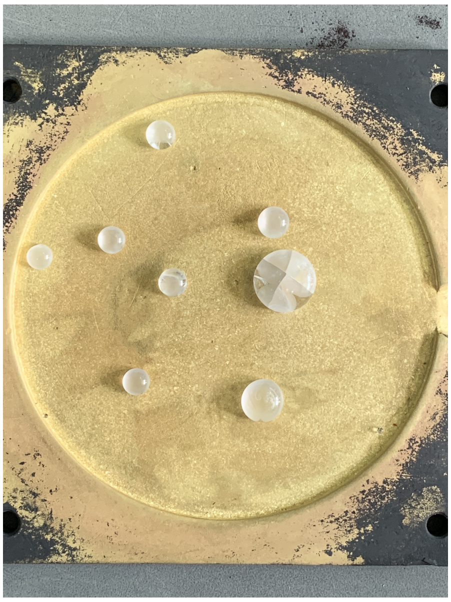

Figure 4.1: LAMGPS glass obtained by melt-quenching method.

4.2 DTA analysis on glass

In the Differential Thermal Analysis (DTA), the sample under study and the inert reference are made to undergo an identical heating ramp. All temperature differences between sample and reference are recorded over time, to detect any thermal-related transformation occurring in the sample. The measurements were carried out taking into consideration a closed system in which were present:

- the sample S, an alumina crucible in which few grams (around 100 mg) of glass bulk and glass powders were put, respectively,
- a reference R, an alumina crucible too, in which the same quantity of an inert material (Al_2O_3) was inserted.

Both crucibles are symmetrically disposed, and layed in a heating chamber. They are controlled by two thermocouples, that detect the variation of temperature. Furthermore, they are connected to a voltmeter able to identify when a temperature variation between the sample S and the reference R occurs, measured in $\mu V\,mg^{-1}$. When a glass is transformed into a glass-ceramic, three different zones are generally expected. Initially, an endothermal behavior can be noted, where the glass transition temperature T_g indicates the start of densification. Subsequently, an exothermic peak defines the crystallization process, in which the crystallization peak represents the maximum velocity. Finally, a new endothermic peak can be observed, either related to a phase transition or to the melting of the main or of a secondary phase constituting the sample. For each sample, DTA analysis (DTA, Netzsch, DTA 404 PC) was performed in the temperature range between 25 °C and 1100 °C at a heating rate of 10 °C min^{-1} in synthetic air.

4.3 HSM analysis on glass powders

The analysis carried out by a heating microscope (HSM) permits to combine the properties of thermal analysis and microscopy. Through an optical microscope, it is possible to perform a quantitative analysis on the glass shrinkage. Moreover, analysis on how the sample changes its form, which corresponds to an area. Also an image analysis was performed, which permits to understand how the powders behave when a heating ramp is applied. The powders are uni-axially pressed, thus obtaining a pellet. The instrument evaluates its dimensional variations (area, height) as a function of temperature. This kind of analysis permits to study the sintering process, since DTA does not provide informations about it, and to identify characteristic temperatures, such as softening, spherical, hemispherical and flow temperature.

The instrument is constituted by a heating furnace, working in controlled atmosphere and water cooled. The glass powders were uniaxially pressed to form a pellet, which was put in the furnace, in contact with a thermocouple. To detect the variation of the sample, it was hit by a light source, which projected the shadows on the opposite side. Its every change was collected by a camera, for each variation of temperature.

HSM analysis (HSM, Hesse Instruments, Heating microscope EM301) thus enabled to follow the sintering behaviour of powders from 25 °C to 1100 °C at a scan rate of 10 °C min^{-1}.

4.4 XRD analysis

The analysis made through X-Ray Powder Diffraction (XRD) permits to understand what is the crystallographic structure of the sample under investigation, examining the nature of crystalline phases formed in the glass-ceramics samples. The analysis consists in the generation of an X-ray source, which irradiates the sample's surface and penetrates it internally. As a result of the interaction with the internal crystalline structure of the material, X-rays are scattered and the diffracted beams are recorded and sent to a software, which plots the intensity of the diffracted peaks as a function of the diffraction angle θ, giving rise to an XRD spectrum as the output for the analysis. The resulting diffractogram gives information about the characterization of the material in terms of crystalline content.

The XRD patterns were recorded (XRD, Panalytical, Xpert3 MRD) at RT using Cu Kα radiation (λ = 0.15406 nm) at a voltage of 40 kV and a current of 40 mA, in the 2θ range of 10°-70°, with a scanning rate of 10° min^{-1}.

4.5 SEM analysis

Examining the surface and morphology can allow to understand how the ionic conductivity of the sample can be influenced. This is due to the fact the transport of ions can be compromised by structural defects, such as graind boundaries, pores and cracks. The interest of this work is to obtain a well cohesive structure, as free of defects as possible.

Scanning Electron Microscope (SEM) is a powerful technique that permits the accurate view in nanometric scale of the glass-ceramic under exam, thus revealing grain size, shape and cohesion. The analysis is based on the principle of scattering of electrons on the surface of sample. The element is put on a holder and inserted into a chamber where a vacuum is generated, in order to prevent the distortion of the measurement, since the electrons can be scattered with air. A filament of tungsten produces a high-energy beam of electrons, which is accelerated by a voltage potential. This flow hits the surface of the sample, showing the structural surface.

Preliminary steps to perform a microstructural characterization through SEM consist of polishing and sputtering. First, the samples were polished under a continuous water flow using different abrasive papers of different grits, in order to make the surface smooth. Precisely, 320, 600, 800, 1200, 2500, and 4000 grits have been used, from the courser to the finer. The next step is characterized by the application of a carbon tape path from the samples to the SEM holder, to create a percolated path. Then, since electrons have high energy, the material needs of a high electronic conductivity, otherwise the scanning can fault. To overcome this, a thin coating of platinum is applied, in order to enhance the electronic conductivity and make the samples conductive, thus creating a Pt/LAMGPS configuration.

SEM microscopy (SEM, Jeol, JCM-6000Plus, BenchtopSEM) was performed in high vacuum and at a voltage of 15 kV.

4.6 EIS analysis

In an electrochemical system, the impedance can be defined as the ratio between the sinusoidal small-amplitude voltage applied and the alternated current flowing. Thanks to the frequency modulating the sinusoidal voltage, the Electrochemical Impedance Spectroscopy (EIS) analysis allows to measure and differentiate the resistances associated to processes in different timescales, such as the bulk and grain boundaries resistances to ion conduction in the samples.

EIS is normally carried out by applying an excitation AC voltage signal, applied at various frequencies, detecting the current output through the sample, thus obtaining which are the main resistive elements and calculating the ionic conductivity. Being

ω the radial frequency, expressed as $\omega = 2\pi f$, the modulated AC voltage, expressed as function of time, has the form:

$$V_{AC} = V_0[cos(\omega t) + jsin(\omega t)] = V_0 e^{j\omega t} \tag{4.4}$$

The impedance vector is characterized by an angle ϕ in phase with voltage. The current response to a sinusoidal voltage input will be a sinusoidal at the same frequency, but shifted in phase of ϕ:

$$I_{AC} = \frac{V}{|Z|} e^{j\omega t+\phi} \tag{4.5}$$

Similar to Ohm's law, the impedance of a system can be calculated as the ratio of of input voltage and output current:

$$Z^* = \frac{V(t)}{I(t)} = \frac{V_a sin(\omega t)}{I_a sin(\omega t + \phi)} = Z_a \frac{sin(\omega t)}{sin(\omega t + \phi)} \tag{4.6}$$

Following the Euler's relationship

$$e^{j\phi} = cos(\phi) + jsin(\phi) \tag{4.7}$$

the complex impedance becomes

$$Z = Z_a e^{j\phi} = Z_a cos(\phi) + jZ_a sin(\phi) = Z' + jZ'' \tag{4.8}$$

where Z' and Z" are real part and imaginary part of complex impedance, respectively. The real part represents the ability of the circuit to resist the flow of electrical current, while the imaginary one represents the ability to store electrical energy.
The system under examination, consisting in a symmetric cell with polarizable (electron blocking) electrodes containing the ceramic electrolyte sample, can be modelled as a circuit made of resistors and capacitors. Usually, a typical Nyquist plot of a LAGP/LATP electrolyte (from which LAMGPS derives) is represented by one or more semi-circles in the high frequency region, and a straight line in the low frequency region. The semi-circles, each represented by a parallel combination of a resistor (R) and a capacitor (C), are due the impedance of bulk and grain boundaries, while the straight line is represented by a capacitor in order to describe the accumulation of charge at the interface between an electrode and an electrolyte.

The frequency at the maximum value of the resulting semi-circle in the plot is given by:

$$\omega_{max} = \frac{1}{CR} \tag{4.9}$$

However, in all real systems, capacitors do not ideally behave, since distribution of currents and electroactive species are present [65]. These capacitors (C) are replaced by a Constant Phase Element (CPE), expressed by the equation 4.10:

$$Z_{CPE} = \frac{1}{(j\omega)^n Q} \tag{4.10}$$

where n is the constant phase exponent ($0<n<1$), and Q replaces C. If n is equal to 1, the CPE equals an ideal capacitor and Q=C. The lower n, and the more depressed the semi-circle. Also the straight line, which is determined by the charge accumulated at electrode/electrolyte interface, can be described as a CPE. In fact, a perfect capacitor C produces a line which makes an angle of 90° with the x-axis (Z') in the Nyquist plot. So, the higher n, the higher is the angle with x-axis. The impedance of a resistor and a CPE in parallel is given by:

$$Z_{R+CPE} = \frac{R}{1 + (j\omega)^n RQ} \tag{4.11}$$

The frequency at the maximum value of the semi-circles is:

$$\omega_{max} = \frac{1}{(RQ)^{1/n}} \tag{4.12}$$

The main issue in an EIS analysis is to find a model with physical meaning to fit the instrumental response. The equivalent circuits can be used to build models or to fit the experimental plots.

4.7 Electrochemical stability

Electrochemical stability window is an important and critical factor, which can determine the practical application in an ion battery. It represents the electric potential range in which the electrode is neither oxidized nor reduced. Therefore, a wide electrochemical window permits to have a large selection of particularly high-voltage cathode materials, which allow for high energy density batteries.

The electrochemical stability window (ESW) of the most conductive sample was evaluated using cells with a configuration of three electrodes, with lithium metal disks and LAMGPS sample as working electrode. The composite electrodes were prepared by a standard method from NMP (N-methyl pyrrolidone, Merk) slurry containing the sample (75 wt.%), conductive carbon (C65, Imerys, 15 wt.%) and PVdF (Solef 6020, Solvay, 10 wt.%). The slurry was deposited onto a Cu foil, dried overnight at RT, cut into 10 mm diameter disks and vacuum dried at 120 °C for one day, prior use to remove water and residual NMP solvent traces. The resulting composite electrodes has a mass loading equal to 3.4 mg cm^{-2}.

Anodic Stability Window (ASW) and Cathodic Stability Window (CSW) were obtained by a Linear Sweep Voltammetry (LSV) test, in the range 0.1 - 3 V for ASW and OCV - 6 V for CSW. Both measurements were carried out at ambient temperature with a scan rate of 0.1 mV s^{-1}.

Chapter 5

Results and discussion

5.1 DTA results

Starting from room temperature, measurements were carried out, obtaining the resulting curve reported in the Fig. 5.1.

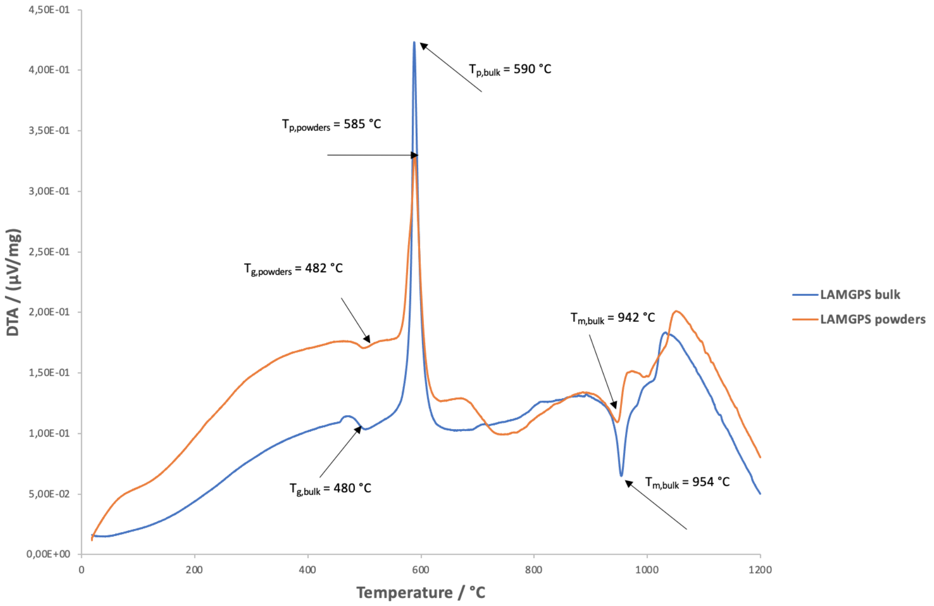

Figure 5.1: Comparison of DTA curves of LAMGPS in the form of bulk and powders.

Regardless of the form of the as-casted glassy samples, either bulk or pulverized,

T_g values were identified at 480 °C in both cases. The glass transition temperature is, in fact, an intrinsic property of the material under examination. Above this characteristic temperature, grains start to nucleate and the glass-to-glass-ceramic transition begins, reaching its maximum crystallization rate in correspondence of the crystallization peak, T_p, which resulted in 585 °C and 590 °C for LAMGPS in its powder and bulk form, respectively. A decrease in the value of T_p (i.e. faster transformation kinetic) while increasing the free surface area of a sample, as for the powder compared to the bulk, indicates that nucleation mainly occurs at a surface.

5.2 HSM results

HSM enabled to study the sintering process of the powders of LAMGPS. Each shape and area variation has been captured over time, starting from room temperature up to 1200°C, with a heating rate of 10 °C min^{-1}. The linear shrinkage is represented on a graph as a function of temperature, as reported in the Fig. 5.2.

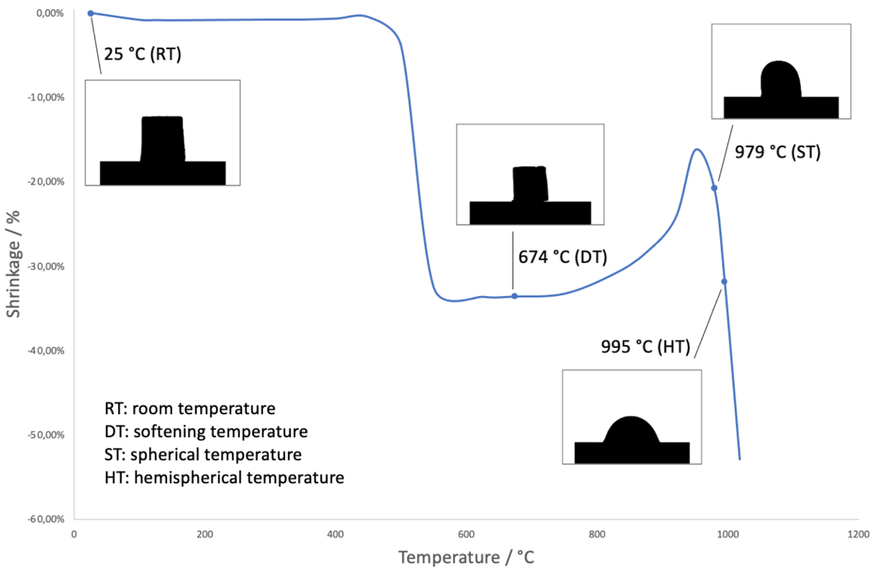

Figure 5.2: HSM curve showing the shrinkage of LAMGPS powders as a function of temperature.

It is possible to distinguish the main characteristic temperatures, which are softening temperature (DT), where the sample starts to become a fluid, spherical temperature

(ST), and hemispherical temperature (HT). The first shrinkage of sample occurs on DT, around 670 °C, and it continues up to around 540 °C, in which the percentage of shrinkage is 33%. After a plateau that arrives until to 760 °C, the melting occurs at around 950 °C, in agreement with the DTA. Moreover, the sample starts to swell at around 700 °C, probably due to evaporation effects of components. Therefore, it becomes essential to treat each sample under this temperature value, in order to prevent the formation of pores that would lead to a decrease of conduction.

5.3 Heat treatments on LAMGPS glass

Based on the previous DTA and HSM results, different heat treatments (tab. 5.1) were tailored and carried out for each sample, to promote the transformation of the as-casted glasses into their glass-ceramics counterparts.

Bulk (devitrification)	**Pellet (sinter-crystallization)**
500 °C 1 h / 750 °C 1 h	750 °C 1 h
500 °C 1 h / 750 °C 6 h	750 °C 6 h

Table 5.1: Heat treatments on LAMGPS glass.

A double-step heat treatment was set for the bulk samples. A first step at 500 °C (T_g + 20 °C) to allow for nucleation to start (nucleation step), and a second one at 750 °C for different treatment times to enable for the growth of the previously nucleated grains (growth step). The nucleation temperature strongly affects the size of the final grains. In particular, if nucleation is performed right above the T_g, few nuclei are likely to form due to the low mobility of the glassy system. On the contrary, by performing nucleation at a temperature corresponding to the maximum crystallization rate (T_p), a significantly higher amount of nuclei is formed. As a consequence, for a given growth step (temperature and duration), few nuclei are likely to grow into larger grains than those resulting from the growth of numerous nuclei. The samples were maintained at 750 °C for different hours, to allow for the formation of different grain sizes. In fact, if the applied temperature is high enough and if the material is stable for the chosen time period, called dwelling time, the growth of crystal is promoted thanks to the supplied thermal energy. This allows the creation of a better-defined crystalline structure, determinant for the resulting ionic conduction.

For the sintering of pellets, an appropriate amount (around 0.35 g) of powders was compacted in a metal die by an uniaxial pressure of 10 MPa. Over the glass transition temperature, since the kinetic energy increases, the pressed powders start to flow viscously. Moreover, necks form along the contact regions between adjacent particles, and grain boundaries form within each neck. In addition, every interstice between particles becomes a pore. As sinter-crystallization process progresses, pores become smaller.

Figure 5.3: LAMGPS glass, LAMGPS glass-ceramic, and LAMGPS pellet.

5.4 EIS results

Before each measurement, both sides of bulk and pellets were polished. Then, the polished samples were sputtered with gold (Au/LAMGPS/Au configuration). The impedance measurements were carried out at different temperatures, with intervals of 10 °C between them, in the range from -20 °C to 80 °C. An AC voltage signal (20 mV) was applied to the samples in the frequency range from 1 MHz to 1 Hz. The real and imaginary parts of the resulting impedance response were plotted in a Nyquist complex plot, showing the contribution of the bulk and grain boundary resistance and the polarization at the electrode/electrolyte interfaces.

For bulk sample treated for 1h at 750 °C, the bulk (R_b) and the grain boundaries (R_{gb}) resistances could not be clearly discerned. Therefore, the spectra were fitted by an equivalent circuit comprising the geometric capacitance (expressed as CPE1) in parallel with the series connection of the total resistance R_{tot} (where R_{tot} =

R_b + R_{gb}) and the capacitance at electrodes/electrolyte interface (expressed as CPE2). The resulting equivalent circuit can be schematized as CPE1/(R_{tot} + CPE2). The total resistance R_{Ttot} was obtained from the low-frequency (right side of the spectrum) intercept of the semicircle with real Z' axis. Regarding the bulk sample treated at 750 °C for 6 hours, the spectra show a semi-circle with a high-frequency intercept (left side of the spectrum) with the Z' axis clearly shifted from the origin. In this case, the equivalent circuit is represented by a resistor (R_b), which corresponds to bulk resistance, in series with a parallel combination of the geometric capacitance (CPE1) and the connection in series of the grain boundaries resistance (R_{gb}) and the capacitance at electrodes/electrolyte interface (CPE2). The equivalent circuit can be schematized as R_b + [CPE1/(R_{gb} + CPE2)]. , where the left intercept with the real Z' axis corresponds to bulk resistance R_b, while the right one corresponds to grain boundaries resistance R_{gb}. The Nyquist plots of impedance of pellets were shaped as those of the bulk sample treated at 750 °C for 6 hours, and were fitted using the same equivalent circuit R_b + [CPE1/(R_{gb} + CPE2)].

The experimental spectra recorded at 20 °C and the fitting curves are shown in Fig. 5.4.

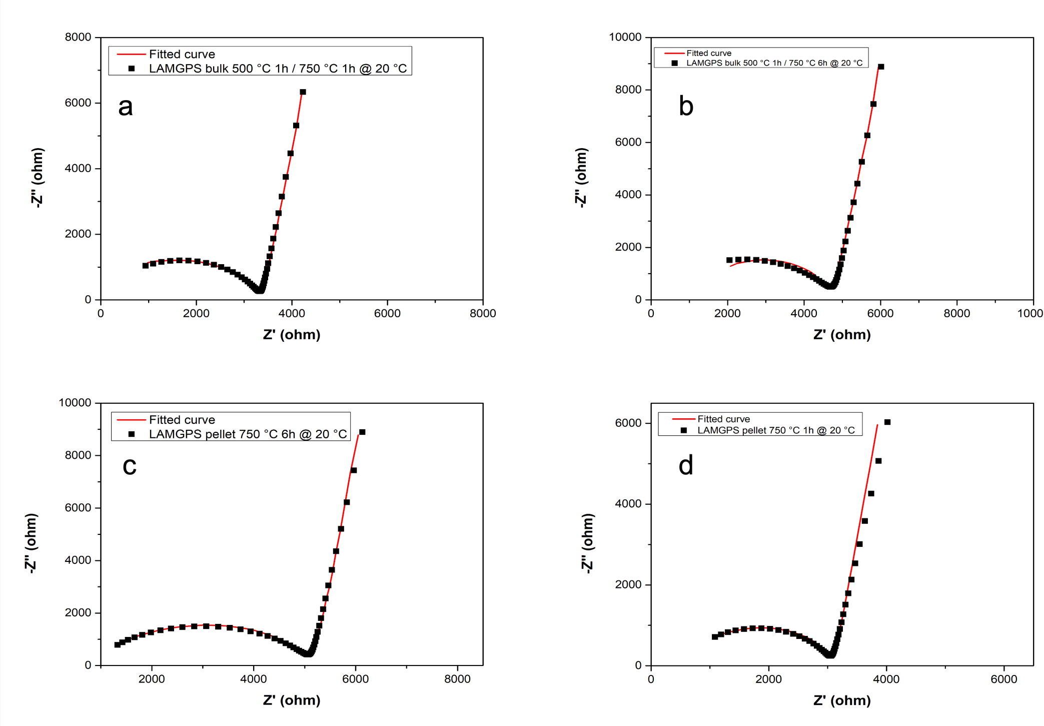

Figure 5.4: Nyquist spectra of bulk heat-treated and sintered LAMGPS at 20 °C. From above: LAMGPS bulk (a,b) and LAMGPS pellets (c,d).

5.5 Ionic conductivity measurement

The ionic conductivity σ_{ion} can be calculated from the values of resistance extracted from the impedance spectra following the Eq. 5.1.

$$\sigma_{ion} = \frac{l}{AR_{tot}} \tag{5.1}$$

where l is the electrolyte thickness, A represents the cross-sectional area, $R_{tot} = R_b + R_{gb}$ is the total resistance including the bulk (R_b) and the grain boundaries resistance R_{gb}. To model the dependency of conductivity upon changing the temperature the following formula can be used:

$$\sigma_{ion} = A \exp\left(-\frac{E_a}{k_B N_A T}\right) \tag{5.2}$$

where k_B is the Boltzmann constant, N_A is the Avogadro number, and T is the temperature.

The experimental data and the corresponding fitting lines are represented in the Arrhenius plot in Fig. 5.5. The fitting procedure permits to calculate the activation energy (E_a) for ion conductivity, and its quality was determined calculating the correlation coefficient R^2 for each sample. The correlation factor values, which are practically equal to 1, confirm that the model is appropriate to describe temperature dependence of the ionic conductivity. At 20 °C, the conductivity values for each sample, and their corresponding activation energies, are in Tab. 5.2.

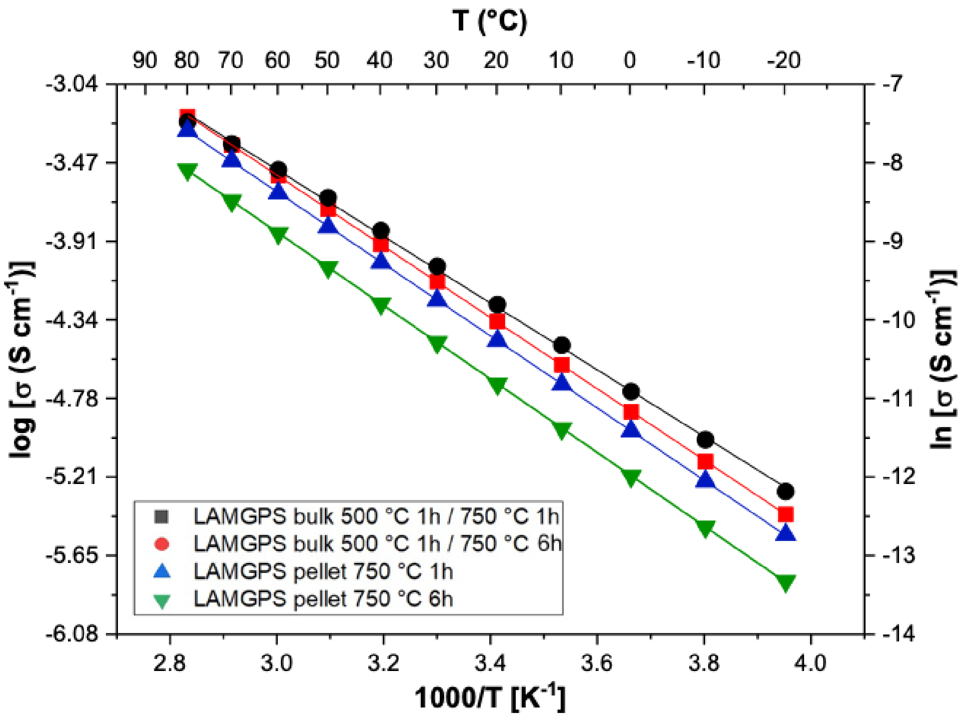

Figure 5.5: Arrhenius plot of σ_{ion} of LAMGPS samples.

LAMGPS sample	σ_{ion} [S cm^{-1}]	E_a [kJ mol^{-1}]
Bulk 500 °C 1 h / 750 °C 1 h	4.45E-05	37.70
Bulk 500 °C 1 h / 750 °C 6 h	5.51E-05	35.24
Pellet 750 °C 1 h	3.48E-05	38.19
Pellet 750 °C 6 h	2.01E-05	38.93

Table 5.2: Ionic conductivity values at 20 °C.

Moreover, to check the effective electron insulating properties of the samples, the electronic conductivity was measured. A chronoamperometric test was carried out, with an applied voltage of 2 V, at 20 °C. The current density as function of time is displayed in Fig. 5.6.

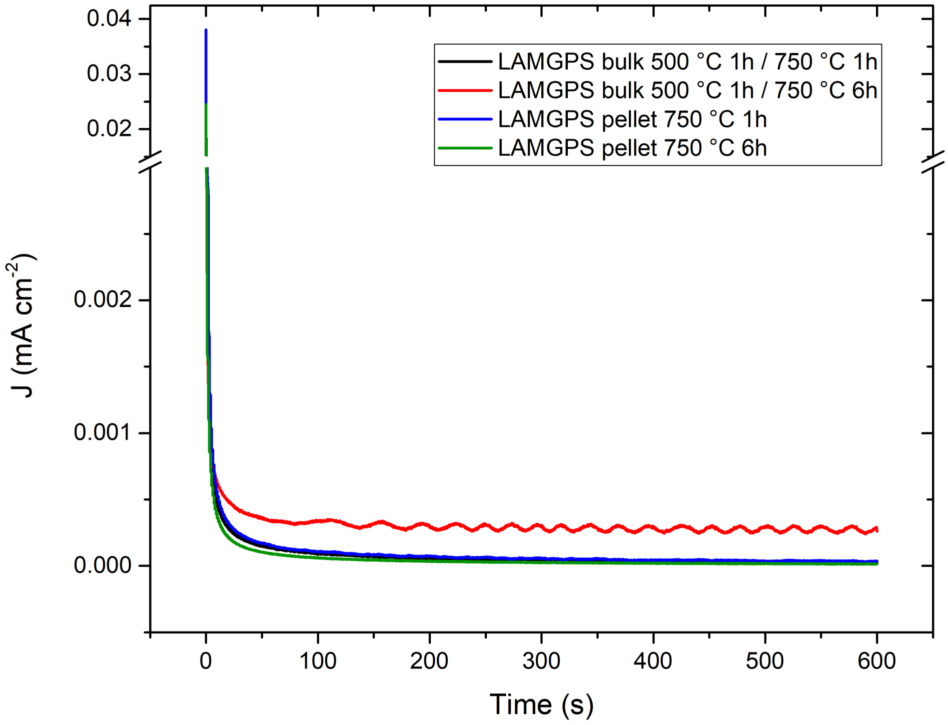

Figure 5.6: Chronoamperometric test diagram for LAMGPS samples.

After about 50 s, the current density reaches a plateau, and the electronic conductivity can be calculated from its value with the following equation:

$$\sigma_e = \frac{lI}{AV} \tag{5.3}$$

where l is the thickness of electrolyte, I is the current, A is the area of gold-sputtered sample, and V is the polarization voltage. For each sample, the results are illustrated in the table 5.3, where the ion transfer number TN_{Li^+} is given by:

$$TN_{Li^+} = \frac{\sigma_{ion}}{\sigma_{ion} + \sigma_e} \tag{5.4}$$

Each value of electronic conductivity is at least 4 orders of magnitude lower than the total conductivity, thus suggesting that the electronic conduction contribution can be considered negligible.

LAMGPS sample	**I [A]**	σ_e **[S cm^{-1}]**	**TN$_{Li^+}$**
Bulk 500 °C 1 h / 750 °C 1 h	3.90E-08	2.96E-09	0.9999
Bulk 500 °C 1 h / 750 °C 6 h	1.25E-07	1.65E-08	0.9997
Pellet 750 °C 1 h	7.14E-08	3.86E-09	0.9999
Pellet 750 °C 6 h	3.64E-08	1.88E-09	0.9999

Table 5.3: Electronic conductivity values of LAMGPS bulk and pellet at 20 °C, after different heat treatment times.

5.6 XRD results

Diffractograms of the most conductive samples are shown in Fig. 5.7. The reflections for each crystalline phase are indicated above the diffraction peaks.

The conductive crystalline phase $LiGe_2(PO_4)_3$ (JCPDS reference code: 00-080-1992; major reflections at 25.151°, 21.318° and 21.459°) was identified as the major phase for both samples. $AlPO_4$ (JCPDS reference code: 01-072-1161; major reflections at 22.435°, 20.759° and 49.708°) secondary insulating phases were also detected for both samples. In this regard, one should consider that the first principal peak of $AlPO_4$, located at 26.435°, is overimposed to the one of the secondary peaks of $LiGe_2(PO_4)_3$ at 26.481°. Overall, no significant difference was observed in terms of secondary phases between LAMGPS bulk and pellet. The lower conductivity value for the pellet is then likely to be ascribed to the sintering process, which is commonly characterized by higher residual porosity compared to the bulk route. This aspect will be verified and discussed in paragraph 5.7.

Partial substitution of Al^{3+} and Mg^{2+} for Ge^{4+}, and Si^{4+} for P^{5+} results in a slight shift of the spectrum towards lower angles, due to the formation of the solid solution. Although the main secondary phase, $AlPO_4$, is nonconductive, it can induce a densifying effect which is beneficial for the ionic conductivity, being its unit cell smaller compared to that of the main conductive phase.

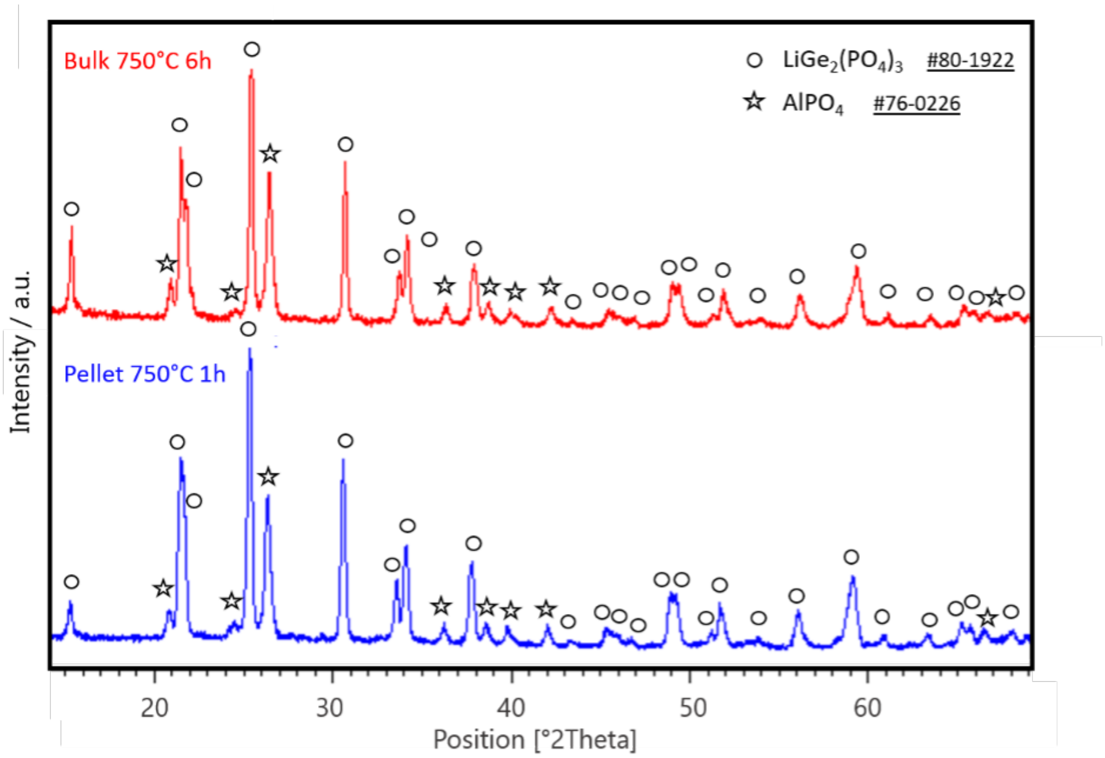

Figure 5.7: XRD patterns of most conductive LAMGPS bulk and pellet.

5.7 SEM images

Although the properest heat treatments have been carried out, some critical issues are present, such as the porosity of the material. The details are illustrated in Fig. 5.8.

Bulk samples showed an enhanced grain size with respect to pellets. From images with a 200x magnification, several pores can be observed, both for fracture and polished surfaces. The porosity explains the low value of ionic conductivity, especially in the case of pellet. At a magnification of 2000x, several grains can be observed. Inside the pores, it is possible to see how the grains are structured, depending on the heat treatment. For short time heat treatments, the number of grains is lower, characterized by a small size. For long time heat treatments, the number of grains enhanced, as well as their dimension. However, they are not well defined, constituting a disordered structure. Therefore, the sintering process remarkably

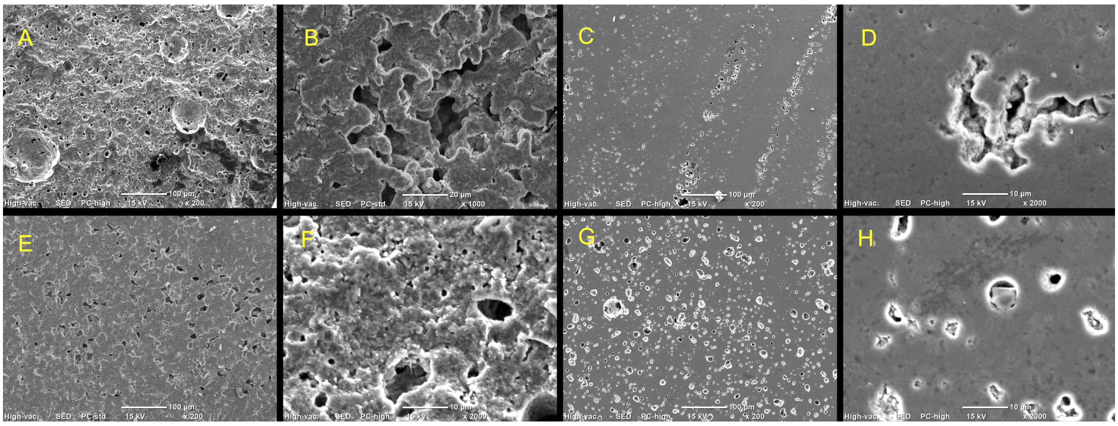

Figure 5.8: SEM micrographs of fracture and polished surface of bulk heat-treated and sintered LAMGPS. From above: bulk heat-treated LAMGPS (A,B,C,D) and LAMGPS sintered pellet (E,F,G,H). From the left: fracture surface (A,B,E,F) and polished surface (C,D,G,H).

influences the microstructures of the sample, thus confirming what X-ray patterns have identified.

5.8 LAMGPS with 10% excess of Li_2CO_3

Although the ionic conductivity of the above-studied composition does not depart from the values reported in literature (one order of magnitude lower), it is necessary to consider that a loss of lithium occurs during casting process. In fact, from the vaporization data of Li_2O [66], at the temperature of casting, a not negligible amount of Li is dispersed. Precisely, at $T_{casting} = 1.350$ °C, and for a period of 2 hours, around 80 mg of lithium oxide are lost. Therefore, to compensate the loss, 10% excess of lithium carbonate Li_2CO_3 was added. Furthermore, considering other possible losses due to board effects inside the crucible and time of process, the hours at 1.350 °C reduced from 2 to 1. Definitely, the steps to form LAMGPS with excess of Li (LAMGPS10) are:

1. From room temperature (RT) to 350 °C, heating rate of 10 °C/min.
2. 30 minutes at 350 °C.
3. From 350 °C to 1.350 °C, heating rate of 10 °C/min.

4. 1 hour at 1.350 °C.

5. Annealing at 480 °C for 2 hours.

Precursors	**# of precursors**	$\%_{mol}$	$\%_{mol,10}$
Li_2CO_3	0.0445	13.39	14.08
Al_2O_3	0.0089	2.68	2.66
$MgCO_3$	0.0059	1.79	1.77
GeO_2	0.0950	28.57	28.34
SiO_2	0.0059	1.79	1.77
$(NH_4)H_2PO_4$	0.1722	51.79	51.37

Table 5.4: Stoichiometric amounts to form 25 g of LAMGPS10 glass.

After annealing process, the resulting glass is shown in Fig. 5.9.

Figure 5.9: LAMGPS10 after annealing.

5.9 DTA on LAMGPS10

The DTA carried out on LAMGPS10 have highlighted an almost equal behaviour of LAMGPS10 compared to LAMGPS, in terms of glass transition temperature. However, the crystallization temperature T_p was shown to increase of about 45 °C (635 °C) in the case of bulk, thus showing a better stability of the glass. As regards T_p of powders, it has remained unchanged. The results are illustrated in Fig. 5.10 below.

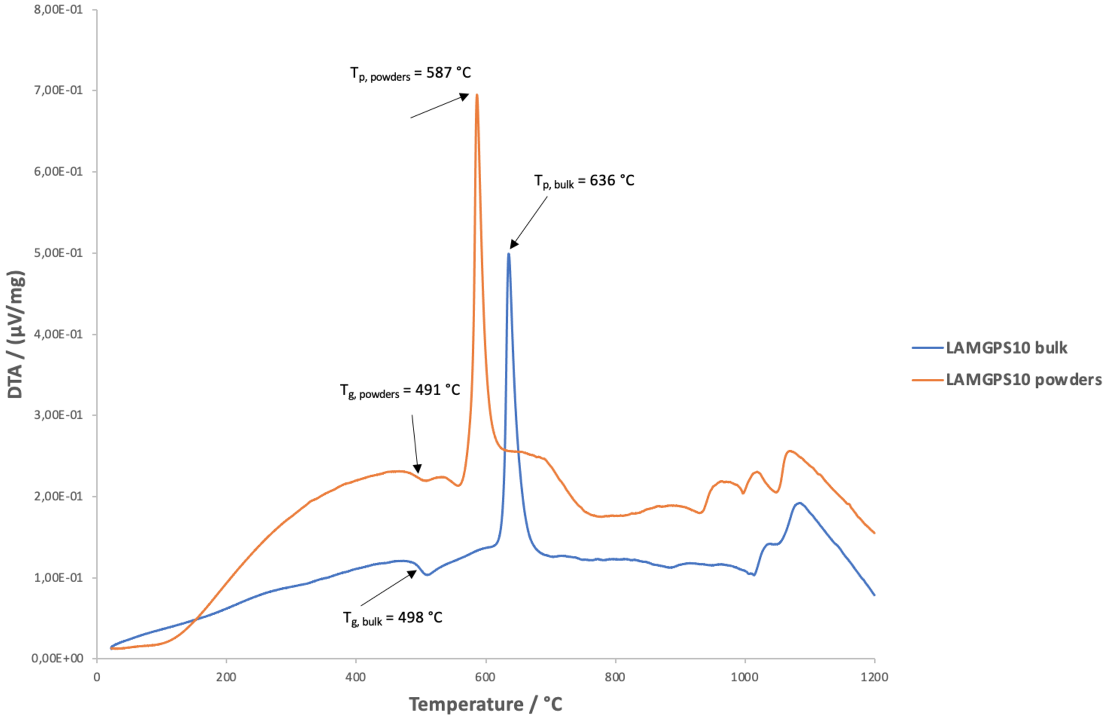

Figure 5.10: DTA results of LAMGPS10.

5.10 HSM of LAMGPS10

As regards HSM, the temperature at which a shrinkage up to 37% occurs, is around 600 °C, showing a better result in comparison to LAMGPS one. Moreover, the length of plateau in which the sample is stable was reduced, thus limiting the temperature range for the heat treatment.

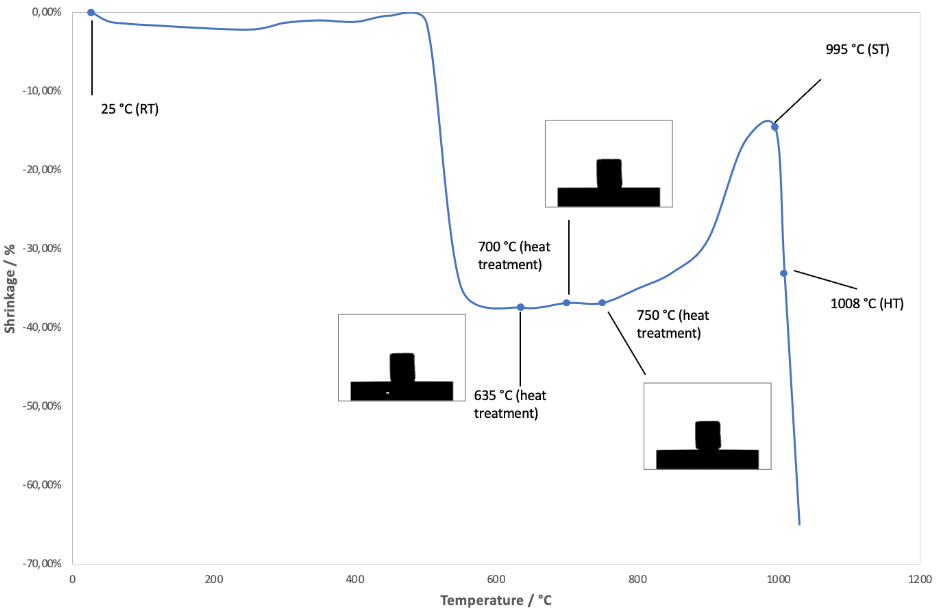

Figure 5.11: HSM diagram of LAMGPS10.

5.11 Heat treatments on LAMGPS10

Examining the results derived by LAMGPS sample characterization, and in particular the micrography, the presence of pores is most likely the main responsible for the low values of conductivity. Therefore, it becomes essential to increase the size of grain, in order to increase σ_{ion}. To do this, the heat treatments have been changed, thus increasing the treatment time up to 12 h for both devitrification and sinter-crystallization processes, according to characteristic temperatures resulting from the new DTA and HSM results shown above. Treatments at peak temperature are useful to the formation of several grains.

Six-hours treatments have been carried out in order to have a comparison with LAMGPS samples.

Bulk (devitrification)	**Pellet (sinter-crystallization)**
635 °C 1h / 700 °C 6 h	750 °C 6 h
635 °C 1h / 700 °C 12 h	750 °C 12 h (2)
515 °C 1h / 700 °C 12 h (1)	-

Table 5.5: Heat treatments on LAMGPS10 glass.

Density values of sample (1) and sample (2) have been obtained through experimental Archimedes method, using the formula

$$d = \frac{w_a - w_w}{w_a} d_w \tag{5.5}$$

where d is the resulting density of the glass-ceramic, w_a and w_w are the weight of sample evaluated in air and in water, respectively, d_w is the density of water (0.997 g cm^{-3}). The resulting densities are reported in Tab. 5.6.

LAMGPS10 sample	**Density [g cm^{-3}]**
Bulk 515 °C 1h / 700 °C 12 h	2.74
Pellet 750 °C 12 h	2.59

Table 5.6: Density values obtained through Archimedes method for LAMGPS10 sample (1) and sample (2).

5.12 LAMGPS10 EIS results

To carry out the analysis, every sample was polished and sputtered with gold. As the same as LAMGPS configuration, the impedance measurements were carried out in the temperature range from -20 °C to 60 °C, with an applied AC voltage signal equal to 20 mV, in the frequency range from 1 MHz to 1 Hz. Impedance spectra of bulk 515 °C 1h / 700 °C 12 h (sample (1)) and pellet 750 °C 12 h (sample (2)) are represented in the Fig. 5.12.

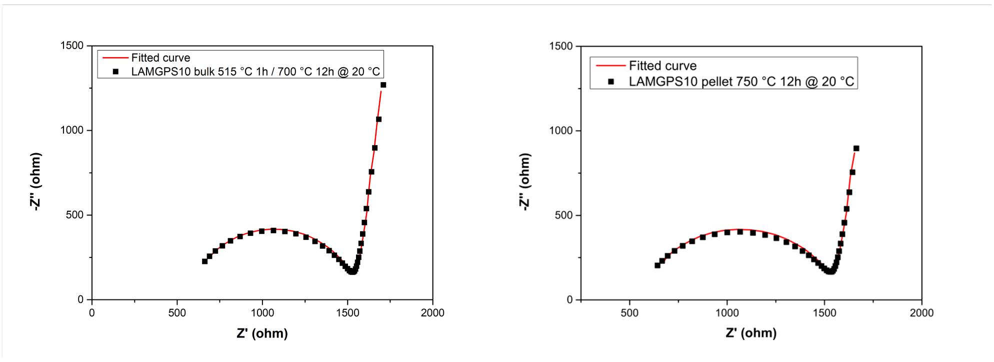

Figure 5.12: Nyquist plots of LAMGPS10 bulk and pellet at 20 °C.

5.13 LAMGPS10 ionic conductivity results

Like LAMGPS composition, every treated sample was subjected to EIS analysis. As expected, the value of ionic conductivity has increased, due to the excess of Li precursor. The results are illustrated in the table 5.7.

LAMGPS10 sample	σ_{ion} [$\mathbf{S\,cm^{-1}}$]	E_a [$\mathbf{kJ\,mol^{-1}}$]
Bulk 635 °C 1 h / 700 °C 6 h	4.81E-05	36.99
Bulk 635 °C 1 h / 700 °C 12 h	4.13E-05	36.09
Bulk 515 °C 1 h / 700 °C 12 h (1)	7.71E-05	25.42
Pellet 750 °C 6 h	2.42E-05	40.37
Pellet 750 °C 12 h (2)	5.12E-05	37.42

Table 5.7: LAMGPS10 ionic conductivity values at 20 °C.

From the above-reported results, the excess of lithium in these samples has lead to an enhancement of conductivity. In particular, bulk 515 °C 1 h / 700 °C 12 h (sample (1)) has the highest ionic conductivity. This is due to lower presence of secondary phases, lower porosity and denser structure, compared to pellets. However, the conductivity of pellet treated 12 hours (sample (2)) arouses interest, because of its possible use in form of powders. Moreover, sample (1) presents an ionic conductivity equal to 1.09 x 10^{-4} $\mathrm{S\,cm^{-1}}$ at 30 °C, which can easily be compared to literature values.

The experimental data and the corresponding fitting lines are represented in Arrhenius plot in Fig. 5.13.

Also for LAMGPS10, electron insulating properties of samples (1) and (2) were measured. A chronoamperometric test was carried out, with the same parameters (2 V, 20 °C) described above. The current density of LAMGPS10 samples is displayed in Fig. 5.14.

Following the equation 5.3, also the electronic conductivities have been calculated, which are reported in the table 5.8, together with the transfer number of Li^+.

Also in this case, electronic conductivities differ from at least 4 orders of magnitude with respect to ionic conductivities, a good ion transport and negligible electronic conduction.

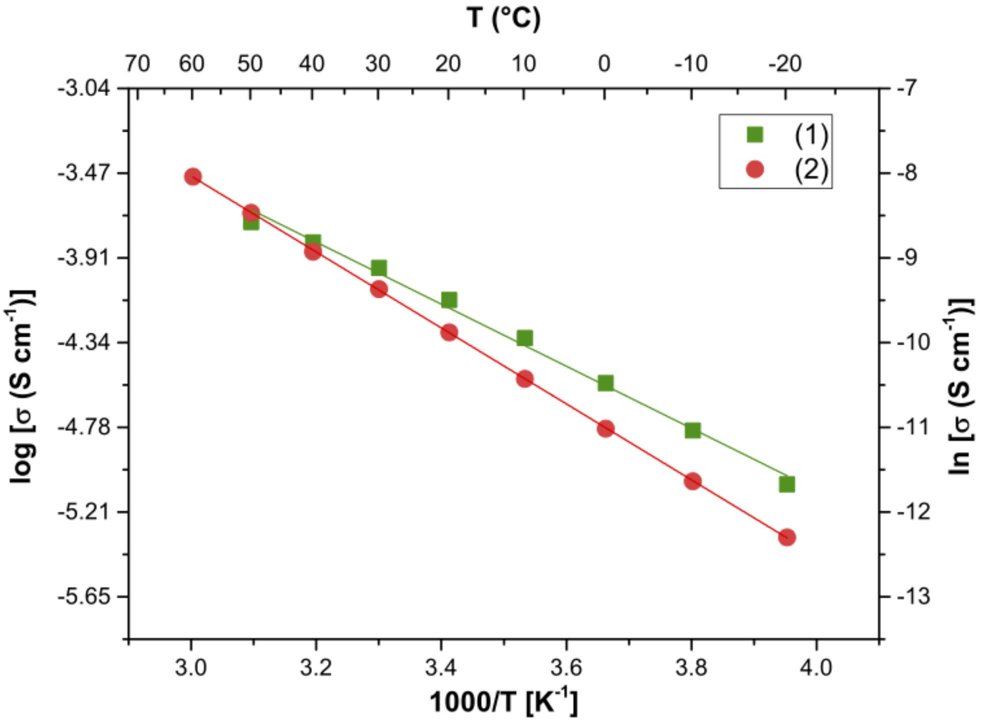

Figure 5.13: Arrhenius plot of σ_{ion} of LAMGPS10 samples (1) and (2).

LAMGPS10 sample	I [A]	σ_e [S cm^{-1}]	TN$_{Li^+}$
Bulk 635 °C 1 h / 700 °C 6 h	1.77E-08	1.02E-09	0.9999
Bulk 635 °C 1 h / 700 °C 12 h	2.56E-08	3.76E-09	0.9998
Bulk 515 °C 1 h / 700 °C 12 h (1)	3.42E-09	3.03E-10	0.9999
Pellet 750 °C 6 h	4.16E-08	2.05E-09	0.9999
Pellet 750 °C 12 h (2)	3.98E-08	1.59E-09	0.9999

Table 5.8: LAMGPS10 electronic conductivity values at 20 °C.

5.14 XRD of LAMGPS10

Compared to LAMGPS, XRD carried out on LAMGPS10 show the presence of $AlPO_4$ secondary exclusively in the sintered sample. For the bulk sample, in fact, no traces of seconday phases are detected and the one and only phase is $LiGe_2(PO_4)_3$ conductive phase. This is in good agreement with the conductivity results shown above for LAMGPS10. The absence of $AlPO_4$ as secondary phase,

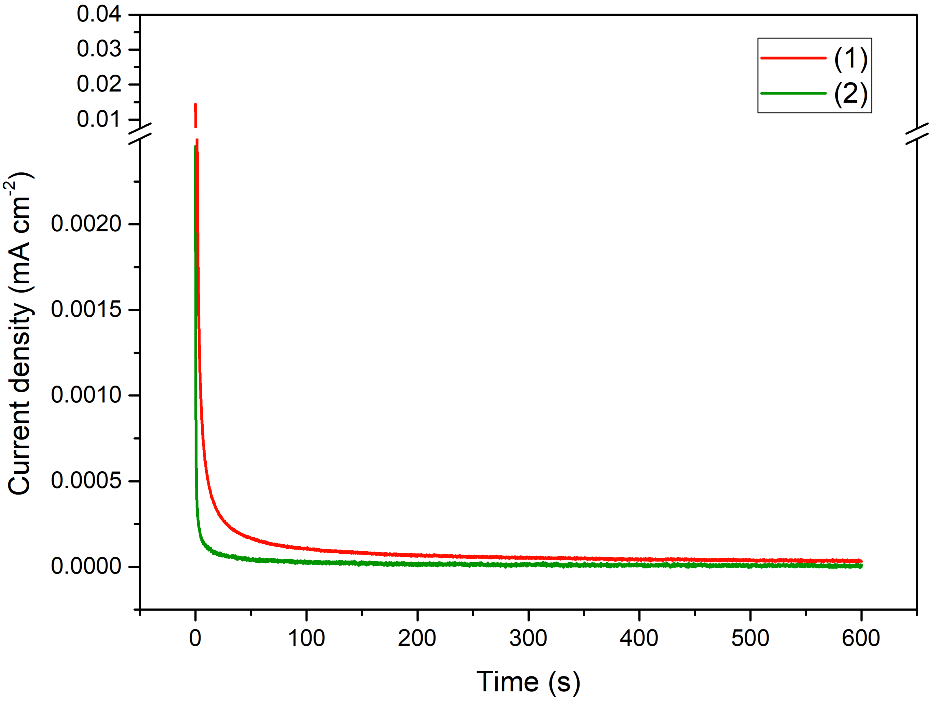

Figure 5.14: Chronoamperometric test diagram for LAMGPS10 most conductive samples.

compared to LAMGPS bulk, is quite certainly a positive effect of the excess of lithium added to the initial composition. By taking into account the Li loss occurring at high temperatures while casting, in fact, stoichiometric amounts of Li are guaranteed in the solid solution and $AlPO_4$, which is known to form in LAGP systems as a consequence of Li loss, is not observed. Temperature might also play a role in this regard, which might explain the reason why $AlPO_4$ is formed in LAMGPS10 pellet (treated at 750°C), despite having the same composition as its bulk counterpart (treated at 700°C). This effect would also responsible for the appearance of unassigned reflections ascribed to non-identified secondary phases in the sintered sample. The increased presence of secondary phases across the two samples could be either identified through an increase in the relative intensity of a given peak or to the appearance of new peaks corresponding to those crystalline phases.

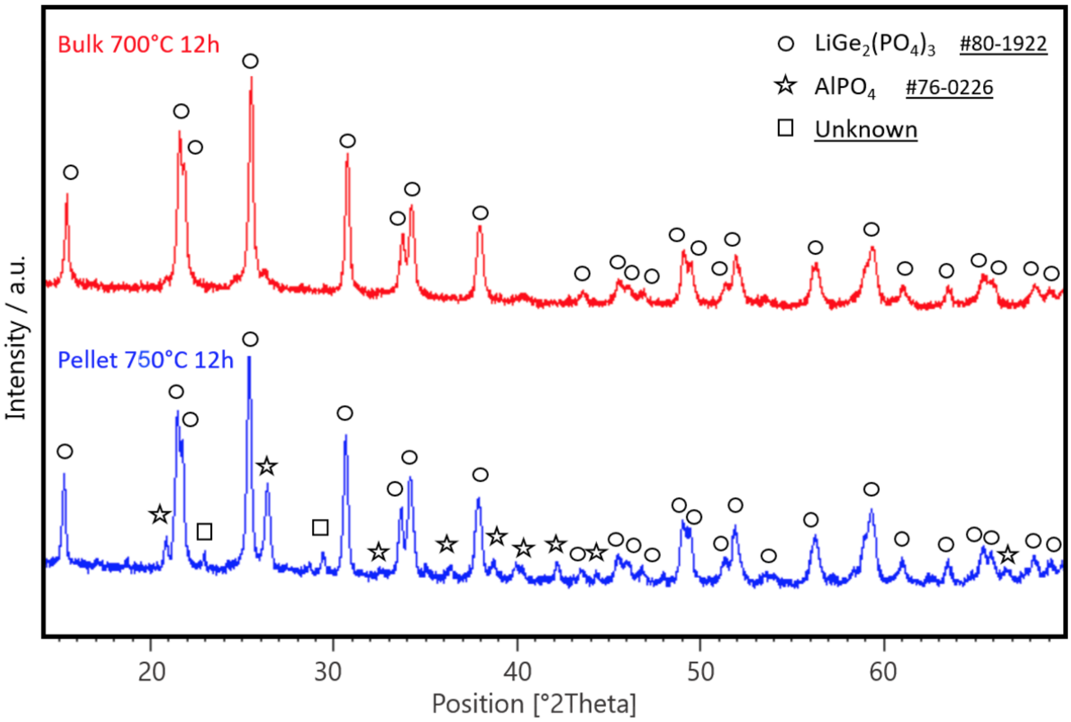

Figure 5.15: XRD patterns of most conductive LAMGPS10 samples, bulk (1) and pellet (2).

5.15 SEM micrographs of LAMGPS10

The most representative images for bulk 515 °C 1h / 700 °C 12h (sample (1)) and pellet 750 °C 12h (sample (2)) are reported below. From these, it was possible to examine the morphological characteristics of the resulting glass-ceramic. Less porous and more compact structure of the bulk compared to the pellet.
From images with a 200x magnification, different pores can be noted, thus explaining the effects they may have on ion conduction. At higher magnifications, precisely at 30kx, an ordered structures of well-defined grains can be observed. In fact, 12 hours heat treatments allowed for an increased microstructural reorganization, resulting in better-defined as well as larger grains, which explains the higher ion conductivities of LAMGPS10 samples than LAMGPS samples. The duration of heat treatment, equal to 12 h, has permitted to have bigger grains, thus obtaining appreciable values of ionic conductivity, with respect to LAMGPS samples. For

the sample (2), images with the same magnification, both for fracture surface and polished surface, are reported. The morphology can be observed in the Fig. 5.16, in which the higher amount of pores may justify a lower value of ionic conductivity, with respect to sample (1).

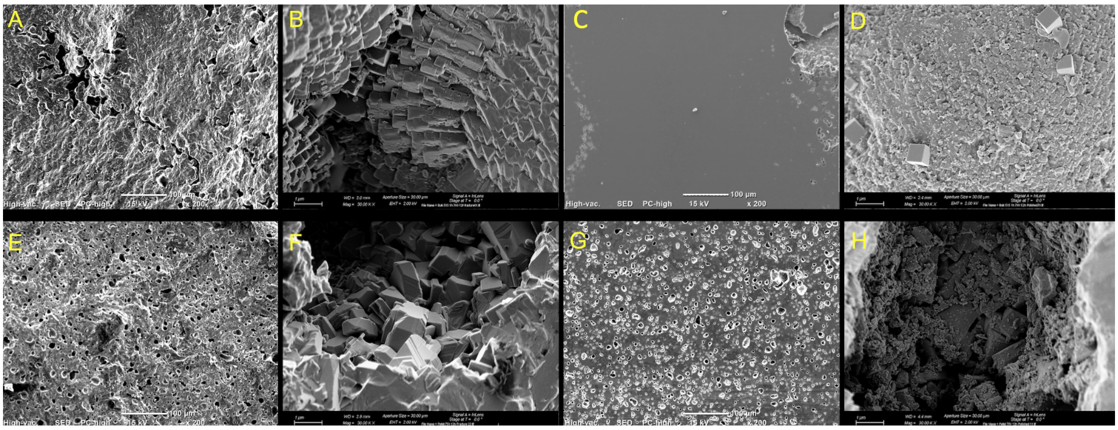

Figure 5.16: SEM and FESEM micrographs of fracture and polished surface of bulk heat-treated and sintered LAMGPS10. From above: bulk heat-treated LAMGPS10 (A,B,C,D) and LAMGPS10 sintered pellet (E,F,G,H). From the left: fracture surface (A,B,E,F) and polished surface (C,D,G,H).

5.16 Electrochemical stability results

The most conductive LAMGPS10 sample (sample (1)) was used as working electrolyte, to determine ASW and CSW. It was pulverized and processed into composite electrodes that contain C65 carbon as additive. To determine the ASW, a cell was prepared, using Li metal as electrode and the bulk, which was sputtered with gold. Between Li and electrolyte, PEO-based polymer electrolyte (PEO-G4) was used as an interlayer, to avoid the reduction of the electrolyte due to the contact with lithium metal. Thus, the proposed configuration was Li/PEO-G4/LAMGPS10/Au. For the ASW, the oxidation process starts at ≈ 4.7 V, at which voltage a negligible oxidation current is generated. The oxidation is followed by an exponential increase, in which the onset voltage of oxidative degradation is equal to 5.3.

As regards the measurement of CSW, it was carried out using LiFTSI 1m in G4 as the electrolyte. Such redox reaction ($Ge^{4+} + 2e^{-} \rightarrow Ge^{2+}$) most likely accounts

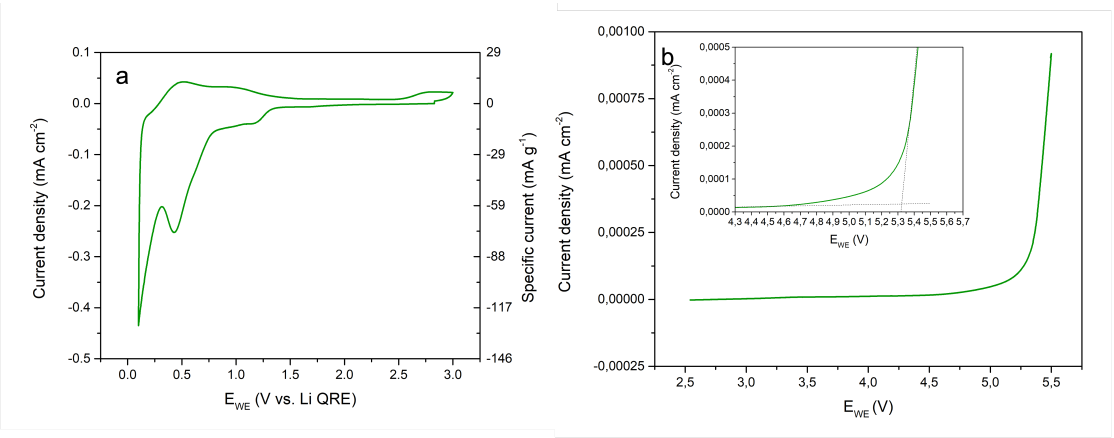

Figure 5.17: LSW scans of electrochemical cells in cathodic/anodic potential ranges. From the left: Cathodic Stability Window (a) and Anodic Stability Window (b).

for reversible processes; nonetheless, it is safer to avoid operating these materials below 1.5 V vs Li in real cell configuration.

Chapter 6

Conclusions and future perspectives

LAMGPS was successfully prepared through a melt-casting technique, starting from analytical reagent-grade chemicals. The melts were then casted on a brass plate and, subsequently, thermally characterized by Differential Thermal Analysis (DTA) and Hot Stage Microscope (HSM). Subsequently, two synthesizing routes were carried out, bulk heat treatment (devitrification) and powder sintering (sinter-crystallization). Bulk devitrification enables to control grain nucleation and growth, to overcome the densification limits intrinsic in the sintering route and to widen the spectrum of possible final sizes and shapes for the materials. Microstructures, ionic conductivity and electrochemical stability windows were then analyzed.
Through Scanning Electron Microscope (SEM) micrographs, the bulk heat treatment showed cohesion between grains, together with several localized pores, while powder sintering showed a less cohesion of grains. Moreover, pellets were characterized by greater porosity, with respect to the bulk heat treated counterpart. Examining its crystalline structure through XRD patterns, the secondary phases was $AlPO_4$, which is nonconductive.
Nyquist plots of samples were obtained by Electrochemical Impedance Spectroscopy (EIS) analysis Au/LAMGPS/Au, thus giving information about the contribution of the bulk and grain boundary resistance and the polarization at the electrode/-electrolyte interfaces. Through Ohm's Law, the ionic conductivity values were

obtained, recording the highest value of 5.51 x 10^{-5} $\mathrm{S\,cm^{-1}}$ at 20 °C for bulk 500 °C 1h / 750 °C 6h. As regards pellets, the highest value was around 3.48 x 10^{-5} $\mathrm{S\,cm^{-1}}$ at 20 °C, which was lower than bulk counterpart, thus confirming the previous analysis.

From the above-obtained results, a new system was characterized, considering an excess of 10% of lithium precursor to the initial composition (LAMGPS10). Same synthesizing routes were carried out, increasing the heat treatment time, in order to enhance the ionic conductivity. SEM images showed more ordered structure of well-designed and bigger grains, due to 12 hours heat treatments. However, some porosity was still present. With the results obtained by EIS, an enhancement of ionic conductivity for the bulk heat-treated was achieved, reaching a value of 7.71 x 10^{-5} $\mathrm{S\,cm^{-1}}$ at 20 °C, and a value of 1.09 x 10^{-4} $\mathrm{S\,cm^{-1}}$ at 30 °C, comparable to literature values. Concerning powder sinter-crystallized samples, the highest achieved value was 5.12 x 10^{-5} $\mathrm{S\,cm^{-1}}$ at 20 °C. These values were justified by XRD results, since secondary phase $AlPO_4$ was not present. The most conductive sample was then subjected to a Linear Sweep Voltammetry (LSW) to determine the Anodic Stability Window (ASW) and the Cathodic Stability Window (CSW), with an optimum onset voltage oxidative degradation equal to 5.3.

Overall, the promising results obtained by LAMGPS10 bulk material may lead to further analysis to its application as working electrolyte in SSBs. In this scenario, new characterization may be considered, by varying the composition through other dopants or additions. Further research should focus on determining the influence of glass particle size (and distribution) on the sinter-crystallization process, and potential exploitation in next-generation 3-D high energy density batteries.

Bibliography

[1] R. Dombrovski. *Renewable energy policies for eco-innovation.* 2015, pp. 260–284. ISBN: 9781782547884. DOI: 10.4337/9781782547884.00021 (cit. on p. 1).

[2] Paris IEA. *World Energy Outlook 2020.* 2020. URL: https://www.iea.org/reports/world-energy-outlook-2020 (cit. on p. 2).

[3] M. Child, C. Kemfert, D. Bogdanov, and C. Breyer. «Flexible electricity generation, grid exchange and storage for the transition to a 100% renewable energy system in Europe». In: *Renewable Energy* 139 (2019), pp. 80–101. ISSN: 18790682. DOI: 10.1016/j.renene.2019.02.077. URL: https://doi.org/10.1016/j.renene.2019.02.077 (cit. on p. 3).

[4] Paris IEA. *Global EV Outlook 2021.* 2021. URL: https://www.iea.org/reports/global-ev-outlook-2021 (cit. on p. 4).

[5] Grand View Research. *Lithium Market Size, Share Trends Analysis Report By Product (Carbonate, Hydroxide), By Application (Automotive, Consumer Goods, Grid Storage, Glass Ceramics), By Region, And Segment Forecasts, 2020 - 2027.* 2020. URL: https://www.grandviewresearch.com/industry-analysis/lithium-market (cit. on pp. 4, 5).

[6] T. M. Gür. «Review of electrical energy storage technologies, materials and systems: Challenges and prospects for large-scale grid storage». In: *Energy and Environmental Science* 11.10 (2018), pp. 2696–2767. ISSN: 17545706. DOI: 10.1039/c8ee01419a (cit. on pp. 4, 6, 9, 10, 12, 13).

[7] V. Pop, H. J. Bergveld, P. H.L. Notten, and P. P.L. Regtien. «State-of-the-art of battery state-of-charge determination». In: *Measurement Science and Technology* 16.12 (2005). ISSN: 13616501. DOI: `10.1088/0957-0233/16/12/R01` (cit. on p. 8).

[8] G. Zubi, R. Dufo-López, M. Carvalho, and G. Pasaoglu. «The lithium-ion battery: State of the art and future perspectives». In: *Renewable and Sustainable Energy Reviews* 89 (2018), pp. 292–308. ISSN: 18790690. DOI: `10.1016/j.rser.2018.03.002` (cit. on p. 9).

[9] M. Santarelli. *Notes from the course Polygeneration and Advanced Energy Systems*. 2019 (cit. on pp. 9, 26).

[10] M. I. Jamesh and A. S. Prakash. «Advancement of technology towards developing Na-ion batteries». In: *Journal of Power Sources* 378 (2018), pp. 268–300. ISSN: 03787753. DOI: `10.1016/j.jpowsour.2017.12.053`. URL: `https://doi.org/10.1016/j.jpowsour.2017.12.053` (cit. on pp. 10, 11, 13).

[11] Q. Li, J. Chen, L. Fan, X. Kong, and Y. Lu. «Progress in electrolytes for rechargeable Li-based batteries and beyond». In: *Green Energy and Environment* 1.1 (2016), pp. 18–42. ISSN: 24680257. DOI: `10.1016/j.gee.2016.04.006` (cit. on p. 12).

[12] K. Xu. «71 ». In: *Chemical Reviews* 104.10 (2004), pp. 4303–4417. ISSN: 00092665 (cit. on p. 12).

[13] F. Meutzner and M. U. De Vivanco. «Electrolytes - Technology review». In: *AIP Conference Proceedings* 1597 (2014), pp. 185–195. ISSN: 15517616. DOI: `10.1063/1.4878487` (cit. on p. 12).

[14] J. Head. «Relative To the Crater Diameter Is Verv Tvoical». In: *Science* 264 (1994), pp. 1–4. URL: `https://science.sciencemag.org/content/264/5162/1115` (cit. on p. 13).

[15] M. Zhao, B. Zhang, G. Huang, H. Zhang, and X. Song. «Excellent rate capabilities of ($LiFePO_4$/C)//LiV_3O_8 in an optimized aqueous solution electrolyte». In: *Journal of Power Sources* 232 (2013), pp. 181–186. ISSN: 03787753. DOI: `10.1016/j.jpowsour.2013.01.026`. URL: `http://dx.doi.org/10.1016/j.jpowsour.2013.01.026` (cit. on p. 13).

[16] J. Y. Luo, W. J. Cui, P. He, and Y. Y. Xia. «Raising the cycling stability of aqueous lithium-ion batteries by eliminating oxygen in the electrolyte». In: *Nature Chemistry* 2.9 (2010), pp. 760–765. ISSN: 17554330. DOI: `10.1038/nchem.763`. URL: `http://dx.doi.org/10.1038/nchem.763` (cit. on p. 13).

[17] I. Hasa, S. Mariyappan, D. Saurel, P. Adelhelm, A. Y. Koposov, C. Masquelier, L. Croguennec, and M. Casas-Cabanas. «Challenges of today for Na-based batteries of the future: From materials to cell metrics». In: *Journal of Power Sources* 482 (2021), p. 228872. ISSN: 03787753. DOI: `10.1016/j.jpowsour.2020.228872`. URL: `https://doi.org/10.1016/j.jpowsour.2020.228872` (cit. on pp. 13, 14).

[18] D. Bin, F. Wang, A. G. Tamirat, L. Suo, Y. Wang, C. Wang, and Y. Xia. «Progress in Aqueous Rechargeable Sodium-Ion Batteries». In: *Advanced Energy Materials* 8.17 (2018), pp. 1–31. ISSN: 16146840. DOI: `10.1002/aenm.201703008` (cit. on p. 14).

[19] Z. Li, D. Young, K. Xiang, W. C. Carter, and Y. M. Chiang. «Towards high power high energy aqueous sodium-ion batteries: The $NaTi_2(PO_4)_3/Na_{0.44}MnO_2$system». In: *Advanced Energy Materials* 3.3 (2013), pp. 290–294. ISSN: 16146832. DOI: `10.1002/aenm.201200598` (cit. on p. 14).

[20] L. Suo, O. Borodin, T. Gao, M. Olguin, J. Ho, X. Fan, C. Luo, C. Wang, and K. Xu. «"Water-in-salt" electrolyte enables high-voltage aqueous lithium-ion chemistries». In: *Science* 350.6263 (2015), pp. 938–943. ISSN: 10959203. DOI: `10.1126/science.aab1595` (cit. on p. 14).

[21] A. A. Zavitsas. «Some opinions of an innocent bystander regarding the Hofmeister series». In: *Current Opinion in Colloid and Interface Science* 23 (2016), pp. 72–81. ISSN: 18790399. DOI: `10.1016/j.cocis.2016.06.012`. URL: `http://dx.doi.org/10.1016/j.cocis.2016.06.012` (cit. on p. 14).

[22] A. Manthiram, X. Yu, and S. Wang. «Lithium battery chemistries enabled by solid-state electrolytes». In: *Nature Reviews Materials* 2.4 (2017), pp. 1–16. ISSN: 20588437. DOI: `10.1038/natrevmats.2016.103`. URL: `http://dx.doi.org/10.1038/natrevmats.2016.103` (cit. on pp. 15, 16, 18, 21, 32).

[23] S. S. Lee, Y. J. Lim, H. W. Kim, J. K. Kim, Y. G. Jung, and Y. Kim. «Electrochemical properties of a ceramic-polymer-composite-solid electrolyte for Li-ion batteries». In: *Solid State Ionics* 284 (2016), pp. 20–24. ISSN: 01672738. DOI: `10.1016/j.ssi.2015.11.020`. URL: `http://dx.doi.org/10.1016/j.ssi.2015.11.020` (cit. on p. 15).

[24] Y. Hu. «Batteries: Getting solid». In: *Nature Energy* 1.4 (2016). ISSN: 2058-7546. DOI: `10.1038/nenergy.2016.42` (cit. on p. 15).

[25] R. DeWees and H. Wang. «Synthesis and Properties of NaSICON-type LATP and LAGP Solid Electrolytes». In: *ChemSusChem* 12.16 (2019), pp. 3713–3725. ISSN: 1864564X. DOI: `10.1002/cssc.201900725` (cit. on pp. 15, 16, 29, 32).

[26] Y. Kato, S. Hori, T. Saito, K. Suzuki, M. Hirayama, A. Mitsui, M. Yonemura, H. Iba, and R. Kanno. «High-power all-solid-state batteries using sulfide superionic conductors». In: *Nature Energy* 1.4 (2016), pp. 1–7. ISSN: 20587546. DOI: `10.1038/nenergy.2016.30` (cit. on pp. 15, 25).

[27] S. Ohno, A. Banik, G. F. Dewald, M. A. Kraft, T. Krauskopf, N. Minafra, P. Till, M. Weiss, and W. G. Zeier. «Materials design of ionic conductors for solid state batteries». In: *Progress in Energy* 2.2 (2020), p. 022001. DOI: `10.1088/2516-1083/ab73dd` (cit. on pp. 16, 17, 24, 25, 27, 29, 32).

[28] Q. Zhao, S. Stalin, C. Z. Zhao, and L. A. Archer. «Designing solid-state electrolytes for safe, energy-dense batteries». In: *Nature Reviews Materials* 5.3 (2020), pp. 229–252. ISSN: 20588437. DOI: `10.1038/s41578-019-0165-5`. URL: `http://dx.doi.org/10.1038/s41578-019-0165-5` (cit. on pp. 16, 18, 19, 22, 24).

[29] C. Zhao, L. Liu, X. Qi, Y. Lu, F. Wu, J. Zhao, Y. Yu, Y. S. Hu, and L. Chen. «Solid-State Sodium Batteries». In: *Advanced Energy Materials* 8.17 (2018), pp. 14–16. ISSN: 16146840. DOI: `10.1002/aenm.201703012` (cit. on pp. 18, 22–24, 32).

[30] A. Unemoto, M. Matsuo, and S. I. Orimo. «Complex hydrides for electrochemical energy storage». In: *Advanced Functional Materials* 24.16 (2014),

pp. 2267–2279. ISSN: 16163028. DOI: 10.1002/adfm.201303147 (cit. on pp. 19, 20, 32).

[31] M. Matsuo, Y. Nakamori, S. I. Orimo, H. Maekawa, and H. Takamura. «Lithium superionic conduction in lithium borohydride accompanied by structural transition». In: *Applied Physics Letters* 91.22 (2007), pp. 5–8. ISSN: 00036951. DOI: 10.1063/1.2817934 (cit. on p. 20).

[32] M. Matsuo and S. I. Orimo. «Lithium fast-ionic conduction in complex hydrides: Review and prospects». In: *Advanced Energy Materials* 1.2 (2011), pp. 161–172. ISSN: 16146832. DOI: 10.1002/aenm.201000012 (cit. on pp. 20, 32).

[33] T. Asano, A. Sakai, S. Ouchi, M. Sakaida, A. Miyazaki, and S. Hasegawa. «Solid Halide Electrolytes with High Lithium-Ion Conductivity for Application in 4 V Class Bulk-Type All-Solid-State Batteries». In: *Advanced Materials* 30.44 (2018), pp. 1–7. ISSN: 15214095. DOI: 10.1002/adma.201803075 (cit. on pp. 21, 32).

[34] H. Maekawa, T. Iwatani, H. Shen, T. Yamamura, and J. Kawamura. «Enhanced lithium ion conduction and the size effect on interfacial phase in Li_2ZnI_4-mesoporous alumina composite electrolyte». In: *Solid State Ionics* 178.31-32 (2008), pp. 1637–1641. ISSN: 01672738. DOI: 10.1016/j.ssi.2007.10.018 (cit. on pp. 21, 32).

[35] J. B. Bates, N. J. Dudney, B. Neudecker, A. Ueda, and C. D. Evans. «Thin-film lithium and lithium-ion batteries.» In: *Solid State Ionics* 135.1-4 (2000), pp. 33–45. ISSN: 01672738. URL: http://www.sciencedirect.com/science/article/pii/S0167273800003271%5C%5Cnhttp://linkinghub.elsevier.com/retrieve/pii/S0167273800003271 (cit. on pp. 21, 32).

[36] D. Zielniok, H. Eckert, and C. Cramer. «Direct correlation between nonrandom ion hopping and network structure in ion-conducting borophosphate glasses». In: *Physical Review Letters* 100.3 (2008), pp. 1–4. ISSN: 00319007. DOI: 10.1103/PhysRevLett.100.035901 (cit. on pp. 21, 32).

[37] B. Fleutot, B. Pecquenard, H. Martinez, and A. Levasseur. «Lithium borophosphate thin film electrolyte as an alternative to LiPON for solder-reflow processed lithium-ion microbatteries». In: *Solid State Ionics* 249-250 (2013), pp. 49–55. ISSN: 01672738. DOI: `10.1016/j.ssi.2013.07.009`. URL: `http://dx.doi.org/10.1016/j.ssi.2013.07.009` (cit. on pp. 21, 32).

[38] Y. Wang, S. Song, C. Xu, N. Hu, J. Molenda, and L. Lu. «Development of solid-state electrolytes for sodium-ion battery-A short review». In: *Elements* 1.2 (2021), pp. 91–100. ISSN: 18115217. DOI: `10.1016/j.nanoms.2019.02.007` (cit. on pp. 21, 24, 25).

[39] Z. Xue, D. He, and X. Xie. «Poly(ethylene oxide)-based electrolytes for lithium-ion batteries». In: *Journal of Materials Chemistry A* 3.38 (2015), pp. 19218–19253. ISSN: 20507496. DOI: `10.1039/c5ta03471j` (cit. on pp. 22, 32).

[40] S. N. F. Yusuf, S. Z. Yusof, M. Z. Kufian, and L. P. Teo. «Preparation and electrical characterization of polymer electrolytes: A review». In: *Materials Today: Proceedings* 17 (2019), pp. 446–458. ISSN: 22147853. DOI: `10.1016/j.matpr.2019.06.475`. URL: `https://doi.org/10.1016/j.matpr.2019.06.475` (cit. on pp. 23, 32).

[41] S. Song, M. Kotobuki, F. Zheng, C. Xu, S. V. Savilov, N. Hu, L. Lu, Y. Wang, and W. D. Z. Li. «A hybrid polymer/oxide/ionic-liquid solid electrolyte for Na-metal batteries». In: *Journal of Materials Chemistry A* 5.14 (2017), pp. 6424–6431. ISSN: 20507496. DOI: `10.1039/C6TA11165C` (cit. on pp. 23, 32).

[42] F. Croce, G. B. Appetecchi, L. Persi, and B. Scrosati. «Nanocomposite polymer electrolytes for lithium batteries». In: *Nature* 394.6692 (1998), pp. 456–458. ISSN: 1476-4687. DOI: `10.1038/28818`. URL: `https://doi.org/10.1038/28818` (cit. on pp. 23, 32).

[43] J. C. Bachman et al. «Inorganic Solid-State Electrolytes for Lithium Batteries: Mechanisms and Properties Governing Ion Conduction». In: *Chemical Reviews* 116.1 (2016), pp. 140–162. ISSN: 15206890. DOI: `10.1021/acs.chemrev.5b00563` (cit. on pp. 24, 26, 27, 32).

[44] M. Tatsumisago, K. Hirai, T. Minami, K. Takada, and S. Kondo. «Superionic conduction in rapidly quenched Li_2S-SiS_2-Li_3PO_4 glasses». In: *Journal of the Ceramic Society of Japan. International ed.* 101.11 (1993), pp. 1283–1285. ISSN: 09129200 (cit. on pp. 24, 32).

[45] N. Kamaya et al. «A lithium superionic conductor». In: *Nature Materials* 10.9 (2011), pp. 682–686. ISSN: 14764660. DOI: 10.1038/nmat3066. URL: http://dx.doi.org/10.1038/nmat3066 (cit. on p. 25).

[46] Z. Zhang et al. «New horizons for inorganic solid state ion conductors». In: *Energy and Environmental Science* 11.8 (2018), pp. 1945–1976. ISSN: 17545706. DOI: 10.1039/c8ee01053f (cit. on pp. 25, 26, 32).

[47] A. Hayashi, K. Noi, A. Sakuda, and M. Tatsumisago. «Superionic glass-ceramic electrolytes for room-temperature rechargeable sodium batteries». In: *Nature Communications* 3 (2012), pp. 855–856. ISSN: 20411723. DOI: 10.1038/ncomms1843. URL: http://dx.doi.org/10.1038/ncomms1843 (cit. on p. 25).

[48] L. Zhang, K. Yang, J. Mi, L. Lu, L. Zhao, L. Wang, Y. Li, and H. Zeng. «Na_3PSe_4: A Novel Chalcogenide Solid Electrolyte with High Ionic Conductivity». In: *Advanced Energy Materials* 5.24 (2015), pp. 2–6. ISSN: 16146840. DOI: 10.1002/aenm.201501294 (cit. on p. 25).

[49] W. D. Richards, T. Tsujimura, L. J. Miara, Y. Wang, J. C. Kim, S. P. Ong, I. Uechi, N. Suzuki, and G. Ceder. «Design and synthesis of the superionic conductor $Na_{10}SnP_2S_{12}$». In: *Nature Communications* 7 (2016), pp. 1–8. ISSN: 20411723. DOI: 10.1038/ncomms11009. URL: http://dx.doi.org/10.1038/ncomms11009 (cit. on pp. 25, 32).

[50] K. B. Hueso, M. Armand, and T. Rojo. «High temperature sodium batteries: Status, challenges and future trends». In: *Energy and Environmental Science* 6.3 (2013), pp. 734–749. ISSN: 17545692. DOI: 10.1039/c3ee24086j (cit. on pp. 26, 32).

[51] W. J. Kwon, H. Kim, K. N. Jung, W. Cho, S. H. Kim, J. W. Lee, and M. S. Park. «Enhanced Li^+ conduction in perovskite Li3XLa2/3-x1/3-2xTiO3 solid-electrolytes via microstructural engineering». In: *Journal of Materials*

Chemistry A 5.13 (2017), pp. 6257–6262. ISSN: 20507496. DOI: 10.1039/c7ta00196g (cit. on pp. 26, 32).

[52] G. Zhao, K. Suzuki, M. Yonemura, M. Hirayama, and R. Kanno. «Enhancing Fast Lithium Ion Conduction in Li_4GeO_4-Li_3PO_4 Solid Electrolytes». In: *ACS Applied Energy Materials* 2.9 (2019), pp. 6608–6615. ISSN: 25740962. DOI: 10.1021/acsaem.9b01152 (cit. on pp. 28, 32).

[53] C. J. Leo, G. V. Subba Rao, and B. V. R. Chowdari. «Effect of MgO addition on the ionic conductivity of $LiGe_2(PO_4)_3$ ceramics». In: *Solid State Ionics* 159.3-4 (2003), pp. 357–367. ISSN: 01672738. DOI: 10.1016/S0167-2738(03)00032-8 (cit. on pp. 28, 32).

[54] H. Y. P. Hong. «Crystal structures and crystal chemistry in the system $Na_{1+x}Zr_2Si_xP_{3-x}O_{12}$». In: *Materials Research Bulletin* 11.2 (1976), pp. 173–182. ISSN: 00255408. DOI: 10.1016/0025-5408(76)90073-8 (cit. on pp. 28, 32).

[55] D. H. Kothari and D. K. K. «Effect of doping of trivalent cations Ga^{3+}, Sc^{3+}, Y^{3+} in $Li_{1.3}Al_{0.3}Ti_{1.7}(PO_4)_3$ (LATP) system on Li^+ ion conductivity». In: *Physica B: Condensed Matter* 501 (2016), pp. 90–94. ISSN: 09214526. DOI: 10.1016/j.physb.2016.08.020. URL: http://dx.doi.org/10.1016/j.physb.2016.08.020 (cit. on pp. 28, 32).

[56] Z. Wu, Z. Xie, A. Yoshida, Z. Wang, X. Hao, A. Abudula, and G. Guan. «Utmost limits of various solid electrolytes in all-solid-state lithium batteries: A critical review». In: *Renewable and Sustainable Energy Reviews* 109 (2019), pp. 367–385. ISSN: 18790690. DOI: 10.1016/j.rser.2019.04.035. URL: https://doi.org/10.1016/j.rser.2019.04.035 (cit. on pp. 28, 29, 32).

[57] M. Illbeigi, A. Fazlali, M. Kazazi, and A. H. Mohammadi. «Effect of simultaneous addition of aluminum and chromium on the lithium ionic conductivity of $LiGe_2(PO_4)_3$ NASICON-type glass-ceramics». In: *Solid State Ionics* 289 (2016), pp. 180–187. ISSN: 01672738. DOI: 10.1016/j.ssi.2016.03.012. URL: http://dx.doi.org/10.1016/j.ssi.2016.03.012 (cit. on pp. 29, 32).

[58] P. Goharian, B. Eftekhari Yekta, A. R. Aghaei, and S. Banijamali. «Lithium ion-conducting glass-ceramics in the system Li_2O-TiO_2-P_2O_5-Cr_2O_3-SiO_2». In: *Journal of Non-Crystalline Solids* 409 (2015), pp. 120–125. ISSN: 00223093. DOI: 10.1016/j.jnoncrysol.2014.11.016 (cit. on pp. 29, 32).

[59] Y. Nikodimos et al. «A new high-Li^+-conductivity Mg-doped $Li_{1.5}Al_{0.5}Ge_{1.5}(PO_4)_3$ solid electrolyte with enhanced electrochemical performance for solid-state lithium metal batteries». In: *Journal of Materials Chemistry A* 8.48 (2020), pp. 26055–26065. ISSN: 20507496. DOI: 10.1039/d0ta07807g. URL: http://dx.doi.org/10.1039/D0TA07807G (cit. on pp. 29, 31, 32).

[60] P. H. Kuo and J. Du. «Lithium Ion Diffusion Mechanism and Associated Defect Behaviors in Crystalline $Li_{1+x}Al_xGe_{2-x}(PO_4)_3$ Solid-State Electrolytes». In: *Journal of Physical Chemistry C* (2019). ISSN: 19327455. DOI: 10.1021/acs.jpcc.9b08390 (cit. on pp. 30, 32).

[61] H. Eckert and A. C. Martins Rodrigues. «Ion-conducting glass-ceramics for energy-storage applications». In: *MRS Bulletin* 42.3 (2017), pp. 206–212. ISSN: 08837694. DOI: 10.1557/mrs.2017.30 (cit. on pp. 30, 32).

[62] Y. K. Shin, M. Y. Sengul, A. S. M. Jonayat, W. Lee, E. D. Gomez, C. A. Randall, and A. C.T. Van Duin. «Development of a ReaxFF reactive force field for lithium ion conducting solid electrolyte $Li_{1+x}Al_xTi_{2-x}(PO_4)_3$ (LATP)». In: *Physical Chemistry Chemical Physics* 20.34 (2018), pp. 22134–22147. ISSN: 14639076. DOI: 10.1039/c8cp03586e (cit. on pp. 30, 32).

[63] Y. Meesala, C. Y. Chen, A. Jena, Y. K. Liao, S. F. Hu, H. Chang, and R. S. Liu. «All-Solid-State Li-Ion Battery Using $Li_{1.5}Al_{0.5}Ge_{1.5}(PO_4)_3$ As Electrolyte Without Polymer Interfacial Adhesion». In: *Journal of Physical Chemistry C* 122.26 (2018), pp. 14383–14389. ISSN: 19327455. DOI: 10.1021/acs.jpcc.8b03971 (cit. on pp. 30, 32).

[64] A. Das, M. Goswami, and M. Krishnan. «Study on electrical and structural properties in SiO_2 substituted Li_2O-Al_2O_3-GeO_2-P_2O_5 glass-ceramic systems». In: *Ceramics International* 44.11 (2018), pp. 13373–13380. ISSN: 02728842. DOI: 10.1016/j.ceramint.2018.04.172 (cit. on pp. 30, 32).

[65] V. F. Lvovich. *IMPEDANCE SPECTROSCOPY - Applications to Electrochemical and Dielectric Phenomena.* 2020, John Wiley Sons, Inc. (Cit. on p. 40).

[66] L. Brewer. «Na and Li Oxides». In: (1955). ISSN: 0022-3654 (cit. on p. 52).

Acknowledgements

ACKNOWLEDGMENTS